An Experimental Study of Matrix Dissolution and Wormhole Formation Using Gypsum Core Flood Tests. Part I: Permeability Evolution and Wormhole Geometry Analysis

Wei Li,[1] Herbert H. Einstein,[1] John T Germaine [2]

[1]Department of Civil and Environmental Engineering, Massachusetts Institute of Technology, Cambridge, MA, USA.

[2]Department of Civil and Environmental Engineering, Tufts University, Medford, MA, USA.

Key Points:

- A new device was introduced in core flood tests to study the evolution of the overall dissolution rate in the rock-fluid system.
- Wormhole growth rate and breakthrough pore volume as functions of the injection flow rate were compared with the relations reported in the literature.
- 3D topological and morphological algorithms were developed to analyze and compare the complex wormhole geometries quantitatively.

This is the author manuscript accepted for publication and has undergone full peer review but has not been through the copyediting, typesetting, pagination and proofreading process, which may lead to differences between this version and the Version of Record. Please cite this article as doi: 10.1029/2018JB017238

Corresponding author: Wei Li, weili08@mit.edu

Abstract

Core flood tests were conducted to study the effect of flow rate on the dissolution of the gypsum rock matrix and the formation of wormholes. An effluent chemistry monitoring system (ECMS) was designed and integrated into a triaxial system to provide continuous effluent concentration measurements, in addition to the pressure and flow measurements during the core flood tests. X-ray computed tomography (CT) was used to study the geometry of the wormholes after the tests. The core flood tests showed agreement with experiments reported in the literature regarding permeability evolution and wormhole breakthrough. By continuously monitoring the effluent concentration, the ECMS advanced the experimental study by showing how the dissolution kinetics evolved with the formation of wormholes. 3D topological and morphological algorithms were developed to analyze the CT data and provide quantitative descriptions for the wormhole geometry. The CT analysis showed that higher flow rates resulted in more complex wormhole geometries regarding the number of wormholes and branches.

1 Introduction

The dissolution of rock minerals is a common process that occurs both under natural conditions (gypsum and limestone karst formations) and under human-induced conditions (carbon dioxide (CO_2) sequestration and oil reservoir acid stimulation). Under these conditions, the flow and dissolution in the rock matrix often induce wormholes, which are long, finger-like channels that form due to the flow and dissolution heterogeneity in the rock matrix. These wormholes become major flow pathways, which significantly increase the permeability of the rock. The formation of wormholes could be a favorable process in oil reservoir acid stimulation, which increases the reservoir permeability and thus oil production. However, it could also be an undesired process from the civil engineering perspective when the wormholes further develop into larger caverns, sinkholes and ground subsidence. It is therefore essential to have a better knowledge of the factors that influence rock matrix dissolution and wormhole formation such as the flow rate.

There have been many experimental studies to investigate the effect of flow rate on rock matrix dissolution and wormhole formation (James & Lupton, 1978; Daccord, 1987; Daccord & Lenormand, 1987; Hoefner & Fogler, 1988; Daccord, Lenormand, & Liétard, 1993; Daccord, Liétard, & Lenormand, 1993; Y. Wang et al., 1993; Taylor & Nasr-El-Din, 2002; Noiriel et al., 2009; Gomaa & Nasr-El-Din, 2010; El-Maghraby & Blunt, 2012;

Sayed et al., 2012; Smith et al., 2013; Hao et al., 2013; Mohamed et al., 2013; Smith et al., 2014; Reynolds et al., 2014; Ghommem et al., 2015; H. Wang et al., 2016; Noiriel & Daval, 2017; Smith et al., 2017; Cai et al., 2018; Menke et al., 2016; Lin et al., 2016; Al-Khulaifi et al., 2018; Menke et al., 2018). In these experiments, core flood tests have been used extensively because of their versatility in controlling and monitoring the confining stress, deviatoric stress, inlet pressure, outlet pressure and deformation during the tests. To study the reactions in the rock-fluid system, researchers often sample and analyze the effluent of the core flood test. Inductively coupled plasma-mass spectroscopy (ICP-MS), ion chromatography (IC) analysis, ion-specific electrode analysis, and pH probe were used to measure the concentrations of the chemical species of interest in the effluent samples (Noiriel et al., 2005, 2009; Mohamed et al., 2013; Smith et al., 2013, 2014, 2017; Al-Khulaifi et al., 2018). In addition, X-ray computed tomography (CT) scans were conducted on the specimen before and after the test to study the change of pore space and the formation of the wormholes (Gouze et al., 2003; Noiriel et al., 2004; Noiriel, 2015; Deng et al., 2015, 2017; Noiriel & Deng, 2018; Yang et al., 2018). These experimental studies have produced a good understanding of the factors that influence the rock matrix dissolution and wormhole formation.

However, the core flood tests conducted so far have limitations in the effluent concentration measurement and CT analysis. During the core flood tests, only a limited number of effluent samples could be collected for analysis, providing limited discrete data for the effluent concentration. Sudden changes in the effluent concentration (Hoefner & Fogler, 1988) could not be accurately captured. In addition, the effluent samples were analyzed under ambient pressure and temperature conditions instead of the pressure and temperature conditions in the specimen. With the change of pressure and temperature, the dissolved gas and solids may come out of solution, which induces errors in the measurements. Additional steps are needed to reduce the errors such as dilution and acidification. For the CT analysis, the geometry of the wormholes have been obtained and described using qualitative descriptors such as “ramified wormholes” and “conical wormholes”. It is difficult to compare the effect of flow rate on the formation of wormholes based on these descriptors.

In the gypsum core flood tests presented in this paper, the aforementioned limitations are addressed with an effluent chemistry monitoring system (ECMS) and 3D topological and morphological CT data analysis algorithms. The paper first presents the spec-

imen preparation process and the material properties resulting from this process (Section 2). Then the experimental setup used for the core flood tests is presented in Section 3, with a detailed description of the ECMS, the CT scan setup, and the 3D topological and morphological algorithms to process the CT data. Section 4 presents the results of the seven core flood tests including pressure data, effluent concentration data, and wormhole geometries. The results are also compared with other core flood test results reported in the literature regarding the wormhole growth rate and breakthrough pore volumes. Section 5 summarizes the innovations in the experimental methods and important findings resulting from these methods. The experimental results are used in the parallel paper (Li et al., 2019) for detailed analysis and modeling.

2 Material

Gypsum is one of the most soluble of the common minerals and rocks throughout the world (Johnson, 2008). The dissolution of gypsum can manifest itself in various ways causing the formation of karst caverns, increasing the permeability of granular zones and enlarging fissures, and attacking cement. Gypsum dissolution is particularly relevant since gypsum also has very low strength and dissolution may eventually lead to failure. In addition, the dissolution kinetics of the gypsum-water system is similar to the limestone-acid system (Daccord, 1987), making it an analogous material for studying acid stimulation. In this study, laboratory cast plaster of Paris was used to prepare gypsum specimen because of its consistency and workability, similar to Daccord's experiments. The plaster used was the NO. 1 Moulding Plaster manufactured by USG Corporation. More than 95% of the material is calcium sulfate hemihydrate ($CaSO_4 \cdot \frac{1}{2} H_2O$), the rest are crystalline silica, limestone and dolomite (NO. 1 Moulding Plasters, 2017). Since the material properties, such as the porosity, are related to the casting process, the specimen preparation is presented before the specific material properties.

2.1 Specimen Preparation

A PVC tube with 35.56 mm inner diameter and 89 mm length was used as a mold for the plaster cast. A mass ratio of 0.6 water to plaster was used, to ensure the plaster is fully hydrated and produce good workability (Einstein et al., 1969). The plaster and water were mixed in a mixer for two minutes, then poured into the mold and vibrated

for another two minutes to achieve uniformity and reduce the air bubbles in the specimen.

After the specimen was cured in a 40 °C oven for one day, the gypsum had enough strength to be unmolded for further drying. The 40°C temperature was proposed by Einstein et al. (1969), to evaporate excess water and prevent the gypsum from dehydrating into hemihydrate or anhydrite. The specimen was further cured at 40 °C for seven days before the test. The specimen was then cut and ground at the two ends to around 83 mm in length for the core flood test. These specimen preparation processes were used and tested by Einstein et al. (1969) to produce specimens with consistent quality.

2.2 Material Properties

The specimen preparation method produced specimens with consistent key material properties such as porosity and initial permeability/hydraulic conductivity (Table 1). The density of the specimen was around 1.22 g/cm^3, obtained by measuring the dimensions and the mass of the specimen. Assuming a specific gravity of 2.33 for the gypsum crystals (Serafeimidis & Anagnostou, 2013), the porosity calculated based on phase relations is in the range of 0.46-0.49.

Mercury intrusion porosimetry (MIP) and scanning electron microscopy (SEM) were also used to characterize the pore space (Giesche, 2006). MIP was performed on a small piece of gypsum sampled from a gypsum specimen (Specimen 6) before cutting it to 83 mm length as a representative of the other gypsum specimens. The pore neck size distribution (PSD) measured using MIP is plotted in Figure 1(a). The pore volume occupied by the pores with a certain pore size (pore neck diameter, as the X-axis) normalized by the total MIP sample volume is the incremental porosity, which is the Y-axis in Figure 1(a). The MIP measurement shows a two-mode PSD, with the minor mode centered around 100 μm and the major mode centered around 2 μm. The minor mode contributes about 0.014 porosity, while the major mode contributes about 0.455, resulting in a total porosity of 0.469. The porosity measured using MIP is thus consistent with the porosity calculated based on phase relations. The 0.46-0.49 porosity is also in the porosity range of 0.40-0.60 for gypsum according to Daccord (1987); Einstein et al. (1969).

Figure 1 (b) is an SEM image of an unpolished gypsum surface. The gypsum crystals show a columnar or reticulated habit and have lengths around 10 μm and diame-

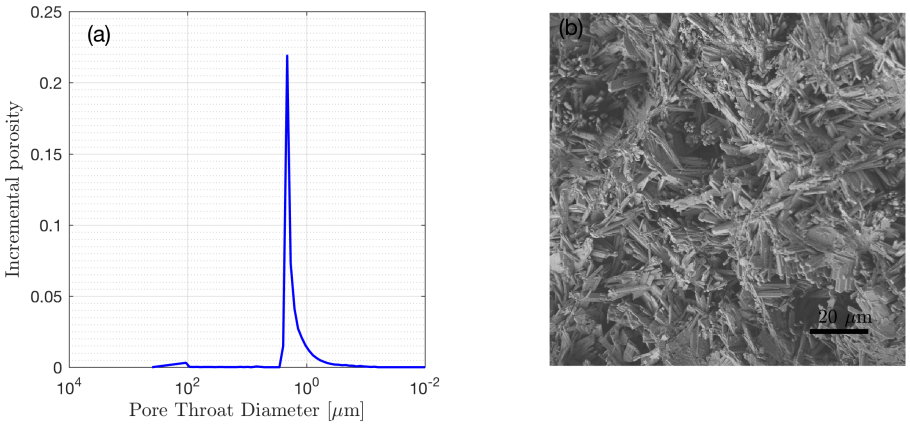

Figure 1. (a) Pore size distribution by mercury intrusion porosimetry. The two peaks of the incremental porosity show a two-mode pore size distribution in the specimen with one mode centered around 100 μm and the other mode centered around 2 μm. (b) SEM image of the specimen. The gypsum crystals show a columnar or reticulated habit and have lengths around 10 μm and diameters around 1 μm.

ters around 1 μm. The pores have a size of several microns, and are the major component of the porosity. The observation using SEM is consistent with the MIP result that the major mode of pore size is around $2\mu m$ (CT scans were also used to study the pore space of the specimen before the core flood test, as will be discussed in Section 3.4).

In the core flood tests, the initial permeability of the material reflects the permeability of the gypsum matrix that has not been affected by the dissolution. The initial permeability of the gypsum specimens at the beginning of the core flood tests is in the range of 21 to 29 mD (Section 4.1), which corresponds to a hydraulic conductivity of $2.06-2.85\times10^{-7}$ m/s (Table 1). The gypsum-water system has a relatively high dissolution rate with the rate coefficient k_r being 7.1×10^{-5} m/s. The solubility of the gypsum in water C_{eq} is 2.6 g/L at 25 $^\circ C$ temperature (Jeschke et al., 2001).

The gypsum-water system was often used as an analogous system for the limestone-acid system (Daccord et al., 1989). To relate the gypsum-water system to the limestone-acid system, the acid capacity number (N_{ac}) is used, which is defined as the mass of solid soluble by the pore fluid per mass of the porous rock matrix (Daccord et al., 1989; Golfier

Table 1. Properties of the seven specimens.

Specimen	1	2	3	4	5	6	7
Flow Rate ($\mu L/s$)	5.00	7.07	10.00	14.14	20.00	28.28	40.00
Length (cm)	8.36	8.59	8.48	8.51	8.33	8.37	8.22
Diameter (cm)	3.53	3.53	3.53	3.52	3.43	3.53	3.53
Mass (g)	100.50	100.70	100.81	99.50	92.77	97.85	97.68
Density (g/cm^2)	1.23	1.20	1.22	1.20	1.21	1.20	1.22
Porosity	0.472	0.485	0.478	0.486	0.483	0.487	0.478
Permeability (mD)	21.3	21.4	27.1	22.4	29.1	21.6	28.1

et al., 2002). The formulation by Daccord et al. (1989) can be adopted for the gypsum-water system as:

$$N_{ac} = \frac{\phi_0 C_{eq}}{(1-\phi_0)\rho_s} \tag{1}$$

where ϕ_0 is the initial porosity; C_{eq} is the equilibrium concentration of gypsum in water; ρ_s is the density of the mineral (refer to Appendix A for the detailed derivation). Given the initial porosity in the range of 0.46-0.49, the equilibrium concentration $C_{eq} = 2.6\ g/L\ =\ 2.6 \times 10^{-3}\ g/cm^3$, and the density of gypsum mineral of 2.33 g/cm^3, the acid capacity number is in the order of 10^{-3}. In comparison to the acid capacity number of a limestone-HCl system, which is in the range of 10^{-3} to 10^{-1} according to Daccord et al. (1989), the gypsum-water system is analogous to limestone-dilute acid or high porosity limestone-acid system.

3 Experimental Setup and Methods

3.1 Computer-Controlled Triaxial System

A computer-controlled triaxial system was used to apply confining pressure on the specimen and inject distilled water through the specimen. The computer-controlled triaxial system was designed and built in the MIT Geotechnical Engineering Laboratory with progressive updates over the past two decades by Sheahan and Germaine (1992); Andersen (1991); Abdulhadi et al. (2011). This system was originally designed for me-

chanical tests on soils and was updated for core flood tests by adding an outlet pressure transducer, upgrading the capacity of the water injection pressure-volume actuator (PVA; this is in essence a syringe pump), and integrating the effluent chemistry monitoring system (ECMS). Figure 2 is a diagram of this computer-controlled triaxial setup. The details of the original triaxial system were discussed in the paper by Sheahan and Germaine (1992).

As shown in Figure 2, the specimen was mounted between the pedestal and ECMS top end cap with porous stones to spread the flow. The porous stones from Gilson® Company are 1.4 inches in diameter and 0.25 inches in thickness. The specimen was sealed with two membrane-sleeves between the pedestal and ECMS top end cap with three O-rings each. The confining pressure was applied with the cell oil using the cell PVA. The axial stress was applied through the ECMS top end cap by a Wykeham-Farrance one-ton capacity, bench-top, screw-driven load frame (powered by a motor with adjustable gear ratios), which is not shown in Figure 2 for simplification.

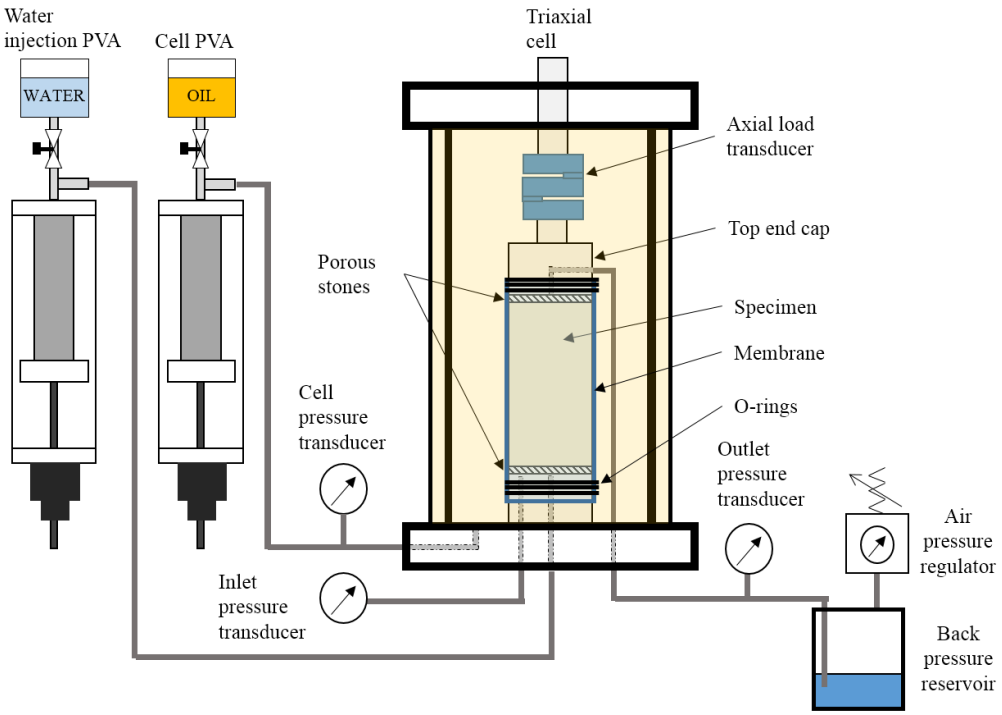

Figure 2. Diagram of the triaxial setup adapted for core flood tests. The parts in the setup are not drawn in the same scale.

3.2 Effluent Chemistry Monitoring System (ECMS)

The ECMS was designed to overcome the limitations of the existing methods discussed in the Introduction. It provides long-term continuous concentration and temperature measurements on the back-pressurized effluent immediately after it exits the specimen. The ECMS consists of a top end cap and a circuit board. Figure 3(a) shows a simplified circuit diagram of the ECMS. The red rectangle indicates the top end cap as a part of the circuit, while the rest of the circuit is integrated into the circuit board. Figure 3(b) is a cross-section view of the detailed design of the top end cap.

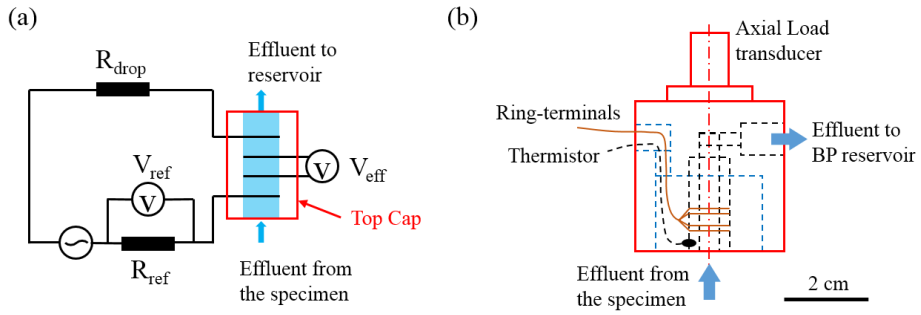

Figure 3. (a) Simplified circuit diagram of the effluent chemistry monitoring system (ECMS). (b) Cross-section of the top end cap with integrated effluent chemistry and temperature sensor.

The ECMS adopted the electric conductivity measurement design proposed by Ramsay (1996) and Adams et al. (2016). The Kelvin sensing method (four-terminal sensing method) was used to measure the electric impedance of the effluent (R_{eff}). Immediately after the effluent exits the specimen, it enters the top end cap where there are four ring terminals on the drainage path. Alternating current (AC) is applied on the two outer terminals to excite the effluent and avoid ion plating. The AC voltages between the two middle ring-terminals and on the reference resistor are measured and converted to direct current (DC) voltage signals by the circuit board. These DC signals are recorded by the data acquisition system as V_{eff} and V_{ref}, respectively. The current in the effluent can be calculated as $\frac{V_{eff}}{R_{eff}}$. Therefore, the electric impedance of the effluent (R_{eff}) can be calculated as:

$$R_{eff} = \frac{V_{eff} \cdot R_{ref}}{V_{ref}}. \tag{2}$$

The ECMS was calibrated to measure the concentration of gypsum-water solutions. The calibration tests were conducted using the setup in Figure 2, except that the specimen was replaced with a dummy stainless steel specimen with a hole along its center axis. Gypsum solutions with known concentrations ($2.6,\ 2.6\times0.25,\ 2.6\times0.25^{-2},\ 2.6\times0.25^{-3}$ and $2.6\times0.25^{-4}\ g/L$) were used as calibration solutions. Each solution was filled in the back pressure reservoir, pushed back towards the top end cap with 70 kPa back pressure and released using a needle valve near the water PVA with a flow rate around 20 $\mu L/s$ till the solution impedance measured by the ECMS reached a steady state value. The needle valve was then closed for 3 minutes to take measurements every two seconds on the solution impedance in the top end cap. The impedance measurements during the 3 minutes are averaged as the solution impedance corresponding to the calibration solution. The measured steady state impedance is stable in the 3 minutes as shown with error bars in Figure 4. The concentrations as a function of the solution impedance based on two calibration tests are plotted in Figure 4. A power law equation was fitted to the data as the calibration equation.

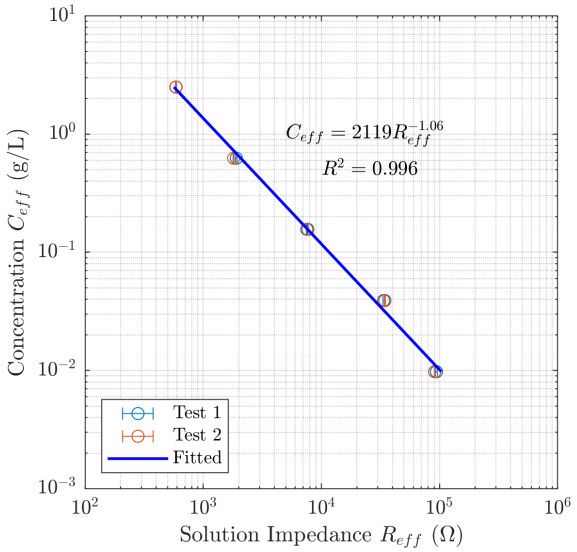

Figure 4. ECMS calibration test results. The calibration equation was obtained by relating the measured solution impedance to its concentration.

A thermistor was also integrated into the top end cap to measure the effluent temperature, as shown in Figure 3(b). By integrating the ECMS into the triaxial system, the effluent concentration and temperature measurement are synchronized with the mea-

surements of the other transducers (pressure transducers, displacement transducers, and load transducers).

During the core flood test, the ECMS measures the concentration and temperature of a small volume of effluent in the top end cap (V_m). This volume of the effluent is continuously replaced by the newly generated effluent. The small volume ($V_m < 0.1\ mL$) in the top end cap provides a fast effluent replacement so that the concentration and temperature are updated fast enough for the continuous measurement. This design detail makes it possible to continuously measure the concentration and temperature of the back-pressurized effluent immediately after it exits the specimen.

3.3 Core Flood Tests

Seven core flood tests were conducted to study the matrix dissolution and wormhole formation as a function of the injection flow rate. Each test used a gypsum specimen that was prepared according to the procedure described in Section 2.1. Each core flood test used one constant flow rate throughout the test. The flow rates were picked based on the tests in the literature. Since the sizes of the specimens from the literature were different, the flow rates (Q) were normalized to the specimen cross-section area as injection fluxes (q), which range from 0.2 to 50 $\mu m/s$ (Hoefner & Fogler, 1988; Mohamed et al., 2013; Noiriel et al., 2016; Smith et al., 2013, 2014, 2017). The flow rates used in our tests ranged from 5 to 40 $\mu L/s$. For the 35.6 mm diameter specimen used in the core flood tests, the injection fluxes thus ranged from 5.4 to 43$\mu m/s$, which were in the range of the tests from the literature. The seven flow rates used for the seven tests were logarithmically spaced as: 5.00, 7.07, 10.00, 14.14, 20.00, 28.28 and 40.00 $\mu L/s$.

The mass and geometric dimensions of the specimens were measured before the experiment to calculate the porosity (Section 2.2). After the specimen was housed in the triaxial cell, a uniform confining stress of 400 kPa was applied. The specimen was then vacuum saturated with a fully-saturated gypsum solution to ensure single-phased flow and prevent specimen dissolution during the saturation process. A back pressure of 70 kPa was applied from the back pressure reservoir (Figure 2) to the specimen for overnight saturation and for the subsequent core flood tests. The temperature measured by the top end cap was used to check if the system had reached temperature equilibrium before the core flood tests.

Around 550 mL of distilled water flowed through the specimen for each test, during which the following parameters were recorded every 10 seconds: inlet pressure, outlet pressure, confining pressure, axial load, axial displacement, injected volume, effluent gypsum concentration and effluent temperature. After the core flood tests, the specimens were dried at 40°C for seven days before taking the mass measurements and CT scan.

3.4 CT Scan and Data Analysis Methods

CT scans of the specimens were taken by the MicroCT system (X-Tek HMXST225) at the Center of Nanoscale Systems at Harvard University. This system uses Mo, W, Ag, or Cu X-ray targets to generate X-rays as high as 225 kV and has a resolution as high as 5 μm. Figure 5 shows the process from scanning to obtaining the 3D binary matrix that represents the void space of the gypsum specimen. The X-rays were generated from a Tungsten target with a voltage of 170 kV and a current of 155 μA and were filtered using a 2.5 mm copper filter. A digital image sensor with 2000×2000 pixels of size 200 μm was used to record each radiograph with 16-bit precision. As shown in Figure 5(a), to fit the specimen image in the image sensor, 4× magnification was used, which resulted in radiographs of the specimen with a resolution of 50 μm (49.514 μm). This resolution is mainly intended for resolving the geometry of the wormholes. The exposure time for each radiograph was 1 second. The specimen manipulation stage was stopped for each radiograph to reduce ring artifacts (Noiriel, 2015). 1955 radiographic projections were taken as the specimen rotated 360° to generate enough data for reconstructing the 3D model of the specimen. Figure 5(b) is one of the 1955 radiographic projections.

The software Inspect-X 3D was used to reconstruct the 3D model of the specimen based on the 1955 radiographic projections. The 3D model is then exported as image stack of horizontal cross-sections of the specimen. Figure 5(c) shows two of the cross-sections of the specimen. Each image in the image stack is the greyscale cross-section of the specimen, with higher brightness representing higher density and lower brightness representing lower density. Since the specimen material is almost pure gypsum, image segmentation for the solid phase and air phase is relatively straightforward (Deng et al., 2016). Image binarization by the global thresholding method is used to provide fast segmentation. On each binary cross-section, 1 (white) represents solid and 0 (black) represents void. Since the void space in the specimen is of main interest for the analysis, the binary cross-sections are inverted, using 1 (white) to represent the void space. The

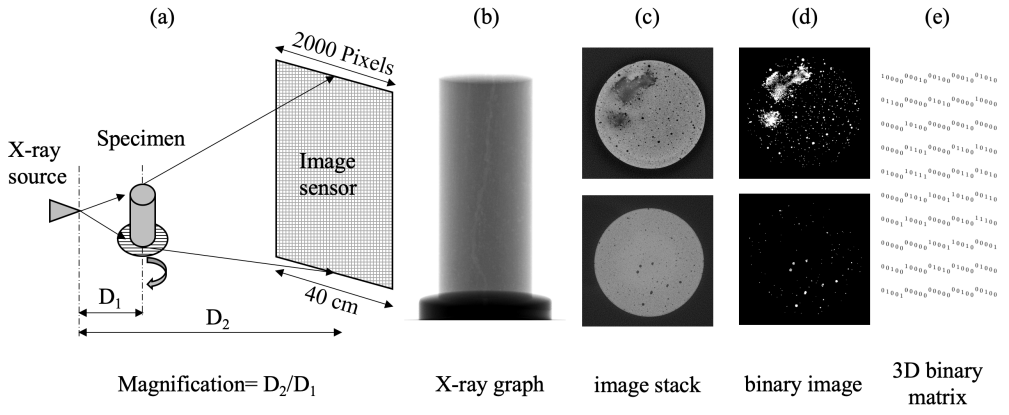

Figure 5. CT scan data acquisition and processing. (a) Schematic of the CT scan setup. (b) One of the 1955 radiographic projections. (c) Image stack of horizontal cross-sections of the specimen. (d) Inverted binary image of the cross-sections with 1 (white) to represent the void space. (d) 3D binary matrix representing the specimen (a $5 \times 5 \times 10$ 3D binary matrix is used as an example).

void space outside of the specimen is also set as 0, as shown in Figure 5(d). The inverted image stacks were then converted to a 3D binary matrix representing the entire specimen. The location of each matrix element corresponds to the location of the voxel in the 3D model of the specimen. By using a binary matrix to represent the 3D specimen model, the amount of data can be reduced from several gigabytes to several megabytes for faster processing and analysis.

In the 3D binary matrix, a pore or wormhole is represented by a cluster of connected elements with value 1. These connected elements can be identified as "connected component" (Russ, 2016). Therefore, each connected component is an individual pore or wormhole with its branches, which consists of a certain number (N_{vi}) of voxels. The volume of the pore or the wormhole (V_i) can be calculated based on N_{vi}:

$$V_i = N_{vi} * 50 * 50 * 50 \ \mu m^3. \tag{3}$$

For the pores, which are roughly spherical, the equivalent diameter (D_i) of each pore can be calculated based on its volume:

$$D_i = \sqrt[3]{\frac{6}{\pi} V_i}. \tag{4}$$

During image binarization, the pores around the size of one voxel may or may not be recognized as the void space. The digital noise from the CT image sensor may also add individual isolated noise voxels. To eliminate these uncertainties from the 3D binary matrix for a reliable analysis, an 8-voxel 3D filter was used to as a cutoff filter. This initial filter also deleted the pores that were represented by less than eight voxels in the CT scan. These pores have equivalent diameters less than $124.07 \mu m$ based on Equations (3) and (4).

3.4.1 Initial pore size analysis

Since the specimens prepared according to Section 2.1 had consistent material properties, only one CT scan was conducted on one of the specimens (Specimen 6) before the core flood test. This CT scan result is assumed to be representative of the other specimens for initial pore space analysis.

After applying the 8-voxel 3D filter, the pores left in the specimen were larger than 124 μm. The total volume of these pores normalized by the volume of the specimen is the porosity contributed by pores larger than 124 μm. Since the pore size (D_i) and volume are known for each pore according to the 3D binary matrix, the pore size distribution for pores larger than 124 μm can be studied. First, the pores are grouped according to their sizes. Then, the total volume of the pores in each group is calculated and normalized to the specimen volume as the porosity contributed by each group of pores. The porosity contributed by each group of pores can be plotted as a function of pore size range of each group as incremental porosity. The 3D reconstruction of the initial pores and the pore size analysis will be presented in Section 4.2.

3.4.2 Wormhole geometry analysis

The 3D binary matrices representing the specimens after the core flood tests were used for the wormhole geometry analysis. Given the initial pore space analysis (Section 4.2), a 1000-voxel 3D filter was used to eliminate the isolated pores and reveal the wormholes in the specimen. The 1000-voxel 3D filter, which had an equivalent diameter of 600 μm, eliminated most of the pores, as shown by the pore size distribution in Figure 8(b). An-

other length filter was applied to eliminate pores that were shorter than 5 mm in the axial direction of the specimen. This filter eliminated isolated pores that were not eliminated by the 1000-voxel 3D filter and wormholes that were shorter than 5 mm. The 1000-voxel 3D filter and 5 mm length filter were chosen so that the isolated pores can be effectively eliminated and the wormholes can be preserved. After the two filters, only wormholes longer than 5 mm were accounted for in the wormhole geometry analysis.

After the filtering process discussed above, the 3D binary matrix is used to reconstruct the wormholes. In this 3D binary matrix, each 1 element represents a wormhole voxel. The binary elements on each $X - Y$ plane represent a horizontal cross-section of the specimen. The wormhole voxel on this plane represents the projections of the wormhole on this plane. Each connected component on this plane with N_{ai} wormhole voxels is a projection with area $A_{ct} = N_{vi} * 50 * 50\ \mu m^2$. Since the wormholes are mostly vertical, their projections on the horizontal cross-section are approximately their cross-sections. This allows one to calculate the equivalent diameter of the wormhole D_e on each plane:

$$D_e = \sqrt{4A_{ct}/\pi} \tag{5}$$

Thus, D_e is a good estimation of the diameter of each wormhole. The software ParaView® was used to produce the 3D rendering of the wormholes and their equivalent diameters in color shown in Figure 6(a). The wormholes resulting from 20 $\mu L/s$ are used as an example to show the 3D rendering.

To quantitatively analyze the complex wormhole geometry in the specimens, 3D topological and morphological algorithms utilizing the MATLAB Image Processing Toolbox were developed to characterize the wormhole complexity. The parameters used to quantify the complexity of the wormholes are: wormhole surface area per specimen volume (S_{whN}), wormhole volume per specimen volume (V_{whN}), the number of wormholes per inlet area (N_{wh}), and the number of branches per specimen length (N_{br}) and tortuosity of the major wormhole (τ_{ac}).

The total surface area of the wormholes (S_{wh} $[m^2]$) is calculated based on the 3D binary matrix of the wormholes. The MATLAB built-in function "bwperim" is used on the 3D binary matrix to find the 3D perimeter of the wormholes. This 3D perimeter represents the surface of the wormholes using just the voxels on the surface of the worm-

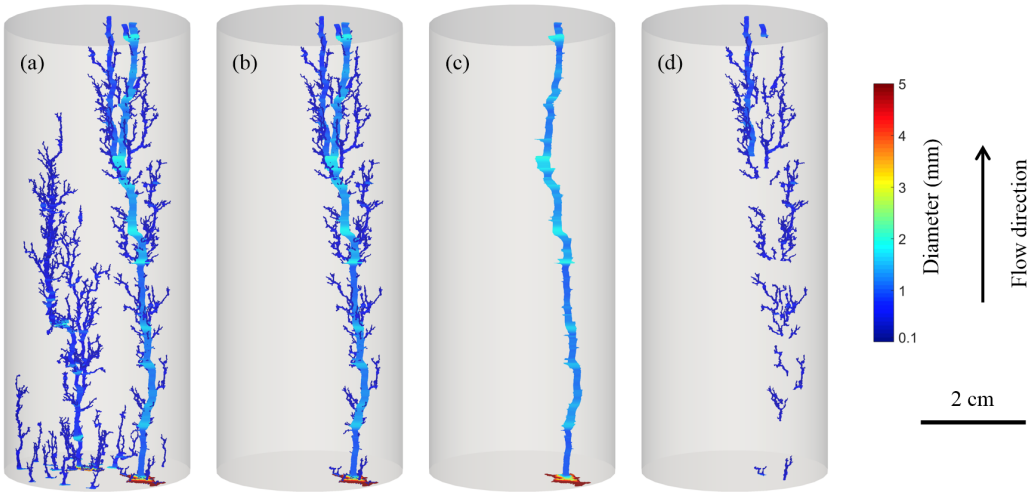

Figure 6. Algorithms to calculate the number of branches. (a). The major and secondary wormholes resulting from the core flood test with $20\mu L/s$ injection flow rate. (b). The major wormhole with its branches. (c) Isolated major wormhole. (d) Isolated branches of the major wormhole.

holes. Each voxel represents the area: 50×50 μm^2. Thus the surface area of the wormholes (S_{wh}) is the number of surface voxels times 50×50 μm^2. S_{wh} is then normalized to the volume of the specimen as the wormhole area per specimen volume (S_{whN} $[m^{-1}]$).

The total volume of the wormholes (V_{wh} $[m^3]$) is also calculated based on the 3D binary matrix of the wormholes. Each of the voxels representing the wormholes has a volume: 50^3 μm^3. Thus the total volume of the wormholes is the number of wormhole voxels times 50^3 μm^3. V_{wh} is then normalized to the volume of the specimen as the wormhole volume per specimen volume (V_{whN} [1]).

The number of wormholes (N_{wh}) can be calculated by totaling the number of connected components in the 3D binary matrix that represents the wormholes. Each connected component represents a wormhole that developed from the inlet of the specimen, which may or may not reach the outlet of the specimen. Since all the wormholes initiated from the inlet of the specimen, the number of wormholes for each specimen is normalized by the specimen inlet area as the number of wormholes per inlet area (N_{whN} $[cm^{-2}]$).

To calculate the number of branches and the tortuosity of the major wormhole, the major wormhole, secondary wormholes and branches need to be differentiated. Figure 6 shows how the morphological algorithms calculate the number of branches step by step. First, the major wormhole with its branches is recognized as the connected component with the largest number of voxels (Figure 6(b)). The major wormhole connecting the inlet and outlet can be obtained by tracing the largest continuous wormhole from the outlet to the inlet(Figure 6(c)). After eliminating the major wormhole from the 3D binary matrix representing the major wormhole and its branches, the branches on the major wormhole then become isolated components (Figure 6(d)). Thus, the number of branches is the number of isolated components in this matrix.

Given the fractal nature of the wormholes (Daccord, 1987), there are secondary branches developing on the branches from the major wormhole. These secondary branches are counted with the one developing from the major wormhole as one branch, when calculating the number of branches. The number of branches on the major wormhole is used to represent the level of branching of the wormholes. Since the wormhole branches on the major wormhole were developed along the flow direction, the number of branches is normalized by the length of the specimen as the number of branches per specimen length (N_{brN} $[cm^{-1}]$).

With the major wormholes extracted as shown in Figure 6(c), the length of the major wormhole (L_t) can be calculated as follows. The coordinates of the center of the major wormhole on each horizontal cross-section are calculated by averaging the coordinates of all the voxels that represent the major wormhole in this cross-section. This averaging algorithm obtains the coordinates of the geometric center of the major wormhole on each cross-section ($x_i,\ y_i,\ z_i$). The distances between the centers of adjacent cross-sections can be summed to obtain the total length of the major wormhole:

$$L_t = \Sigma_{i=2}^{N} \sqrt{(x_i - x_{i-1})^2 + (y_i - y_{i-1})^2 + (z_i - z_{i-1})^2}. \tag{6}$$

The tortuosity τ of the major wormhole can also be calculated:

$$\tau = \frac{L_t}{L_s}, \tag{7}$$

where L_t is the length of the major wormhole, and L_s is the length of the specimen. This definition tortuosity (Equation 7) accounts not only for the local tortuosity of the major wormhole but also the overall inclination from the flow direction.

The 3D topological and morphological algorithms discussed above introduced parameters to characterize the complexity of the wormhole geometry. The normalized parameters S_{whN}, V_{whN}, N_{whN} and N_{brN} are defined so that wormhole geometry can be compared with other tests with different sizes of specimens. For example, the number of wormholes is normalized to the inlet area because all the wormholes initiated from the inlet. If there are other tests using bigger or smaller specimens, the same normalization methods can be applied so that the results can be compared with the results of the core flood tests. These parameters are used to study the effect of flow rate on the complexity of the wormhole geometry in Section 4.3.

4 Results and Discussion

4.1 Pressure and Concentration

The pressure difference between the inlet and outlet (ΔP) and the effluent concentration measured by the ECMS (C_{eff}) for the seven tests are plotted in Figure 7. The injected pore volume (V_p) is calculated for each test as the X-axis. It is defined as the injected volume ($V_{inject} = Q \cdot t$) normalized by the initial pore volume of the specimen V_{pore}, $V_p = Q \cdot t / V_{pore}$. In a core flood test where the initial pore volume V_{pore} and flow rate Q were constants, the injected pore volume (V_p) can also represent a dimensionless linear time coordinate. During each test, the flow rate was kept constant, while the pressure difference (ΔP) and effluent concentration (C_{eff}) changed due to dissolution. These two parameters reflect the evolution of the rock-fluid system during the core flood test.

For each of the seven tests, the pressure difference between the inlet and outlet (ΔP) was the highest, initially, then decreased close to zero, and stayed there for the rest of each test. The initial pressure difference in each test is used to calculate the initial permeability of the specimen, as listed in Table 1. The pressure difference (ΔP) decreased linearly with V_p before a sudden drop close to zero, as shown in Figure 7. The linearly decreasing behavior of ΔP was consistent with the observations in the tests by Daccord et al. (1989). The sudden drop in ΔP observed in each test was an indication of worm-

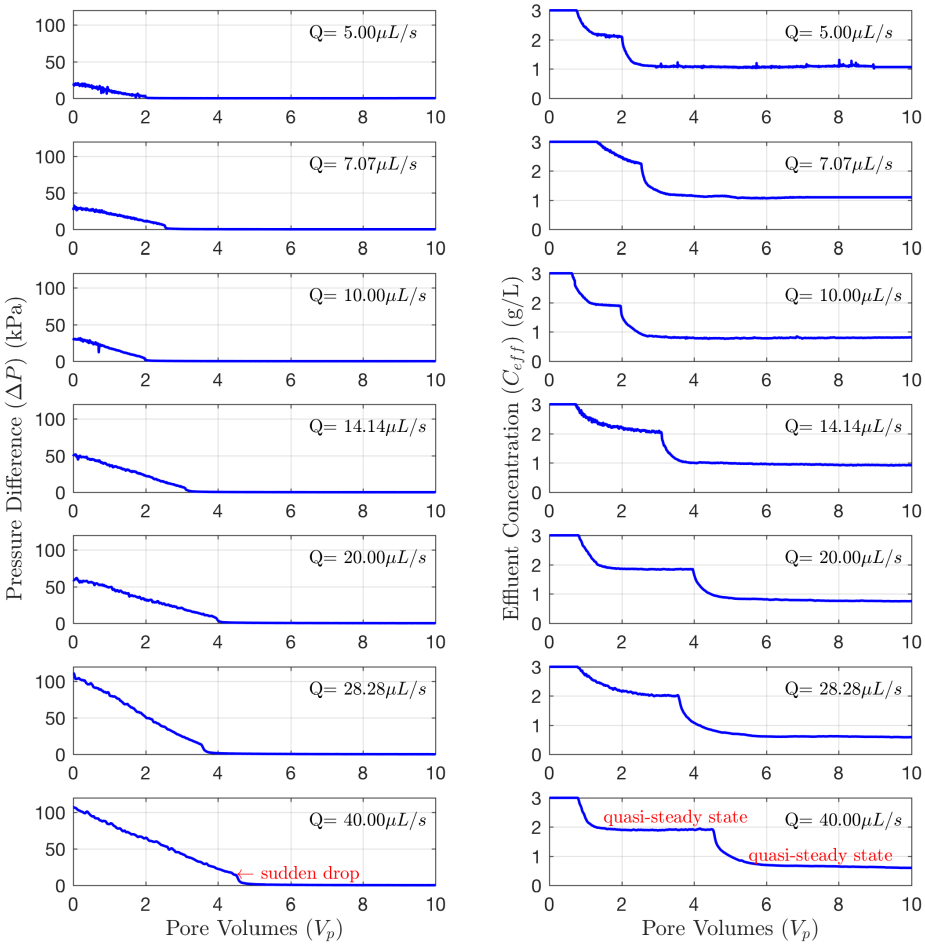

Figure 7. Monitored pressure difference between the inlet and outlet and effluent concentration during the core flood tests.

hole breakthrough since the permeability of a wormhole was much higher than that of the porous medium (Daccord et al., 1989). Detailed analyses of the pressure data and comparison with the previous work are presented in Section 4.4.

Since the ECMS was only calibrated for the concentrations ranging from 0.01g/L to 2.6 g/L, the beginning part of the curve where the concentration is greater than 3 g/L is plotted as 3 g/L in Figure 7. The initial high concentration was a result of the overnight saturation when the back pressure forced the residual air in the pores into the solution and increased the fluid electric conductivity. The fluid with high electric conductivity was then pushed out by the newly injected distilled water and measured by the ECMS. After the initial high concentration, the effluent concentration decreased and reached its first quasi-steady state value. Then it dropped at the same "time" (V_p) when the pres-

sure difference dropped close to zero. Finally, the effluent concentration reached another quasi-steady state value. The evolution of the effluent concentration indicates the evolution of the dissolution kinetics during the core flood test. The analysis and modeling of the effluent concentration will be discussed in more detail in the parallel paper (Li et al., 2019).

The sudden decreases of the pressure difference (ΔP) and the sudden drop of effluent concentration (C_{eff}) occurred at the same "time" (V_p), as shown in Figures 7. A similar phenomenon was also observed by Hoefner and Fogler (1988) through effluent sampling and pH measurements in their core flood tests with a limestone-acid system. This sudden decrease of ΔP corresponds to the change in the hydraulic properties of the rock-fluid system, while the simultaneous sudden decrease of C_{eff} corresponds to the change in the overall dissolution kinetics in the rock-fluid system. They are both induced by wormhole breakthrough. Figure 7 shows that with the continuous concentration measurements by the ECMS, the evolution including sudden changes in the dissolution rate of the rock-fluid system can be captured.

4.2 Initial Pore Space Analysis with CT data

As discussed in Section 3.4.1, Specimen 6 before the core flood test was studied using CT scan for initial pore space analysis. The 3D binary matrix representing Specimen 6 before the core flood test was processed following the descriptions in Section 3.4.1. After applying the 8-voxel 3D filter, there were 97,330 pores left in the specimen that were larger than $124\mu m$. The total volume of these pores normalized by the volume of the specimen is the porosity 0.0092. This indicated that the porosity contributed by pores larger than $124\mu m$ was 0.0092. The specimen and the pores are reconstructed in Figure 8(a). The reconstructed pores are isolated from each other and distributed uniformly in the specimen, which does not provide a preferred flow path.

The pores reconstructed based on the CT scan show a pore size distribution centered around $300\mu m$ and contribute to a porosity of 0.0092 in total. The pore size distribution measured by MIP is also plotted in Figure 8(b) for comparison. Since MIP has limited resolution for large pores, the data point for the pore size around $100\mu m$ represents the incremental porosity of pores larger than $100\mu m$. The pore size distributions measured using CT scanning and MIP agree with each other given that the MIP mea-

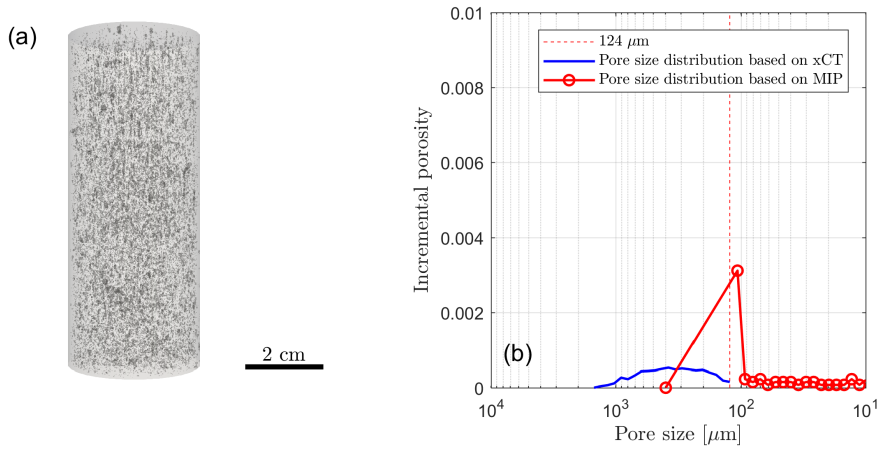

Figure 8. Initial pore space analysis. (a) 3D reconstruction of initial pores larger than 124.07μm. (b) Pore size distribution based on CT data.

sured the pore neck sizes (Giesche, 2006) instead of the equivalent pore sizes and that the CT scan only resolved part of the minor mode of the MIP results.

The initial pore space analysis discussed above studied the initial pores in the specimen that had equivalent diameters larger than 124 μm. The analysis showed that the initial pores were isolated from each other and distributed uniformly in the specimen, which did not provide a preferred flow path. The pore size distribution based on this analysis matched the result of MIP. The results also provided a reference for the scale of the pore sizes when filtering the initial pores to study the wormhole geometry after the core flood tests.

4.3 Quantitative Wormhole Geometry Analyses

The algorithms described in Section 3.4.2 are used to reconstruct the wormholes resulting from different flow rates as shown in Figure 9. The specimens were reconstructed in the same position as they were housed in the triaxial system, i.e., flow entered the specimen from the bottom and exited from the top. Each specimen has one major wormhole, which has the largest diameter connecting the inlet and outlet of the specimen as indicated with warmer colors. The diameter of the major wormhole is in the range of 1 mm to 2 mm. The inlets of the wormholes are larger than the rest of the wormholes. This is caused by the non-uniform dissolution along the wormholes, as discussed in other studies (H. Wang et al., 2016; Smith et al., 2013, 2017; Li & Einstein, 2017). There are sev-

eral secondary wormholes in each specimen, which developed at the inlet of the specimen. Along the major and secondary wormholes, branches also developed producing a tree-like geometry (Daccord, Lenormand, & Liétard, 1993). The wormholes in Figure 9 shows a generally accepted trend that higher flow rates result in more secondary wormholes, and more branches on the wormholes (Daccord, Lenormand, & Liétard, 1993; Fredd & Fogler, 1998; Budek & Szymczak, 2012).

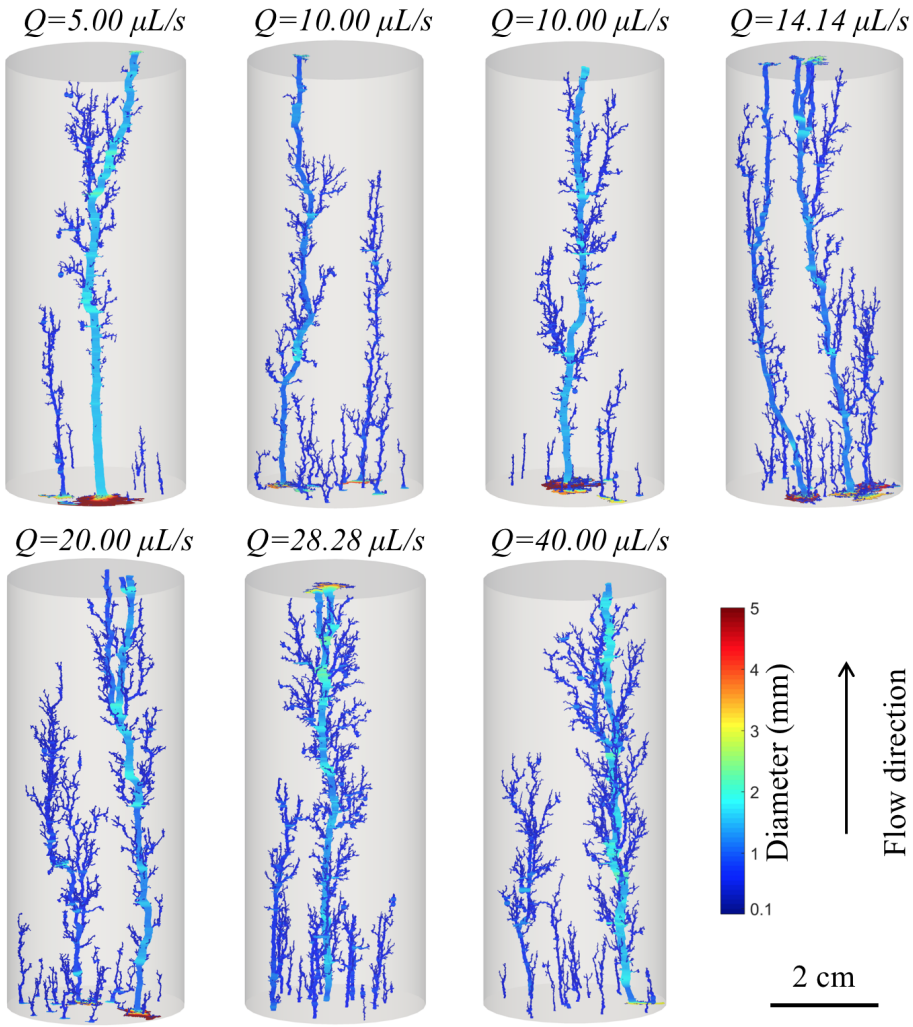

Figure 9. 3D reconstructions of the wormholes in each specimen. The wormholes show that higher flow rates result more complex wormhole geometries.

Based on the 3D wormhole geometry analysis algorithms, the parameters that characterize the wormhole geometry are calculated for the wormholes in the seven specimens. Recall that these parameters are: wormhole surface area per specimen volume (S_{whN}),

wormhole volume per specimen volume (V_{whN}), number of wormholes per inlet area (N_{wh}), the number of branches per specimen length (N_{br}), and tortuosity of the major wormhole (τ_{ac}). These parameters are already normalized to their corresponding dimensions. The injection flow rate is also normalized by the specimen cross-section area as injection flux (q). These parameters are plotted in Figures 10 and 11 to study the effect of injection flux on the wormhole characteristics.

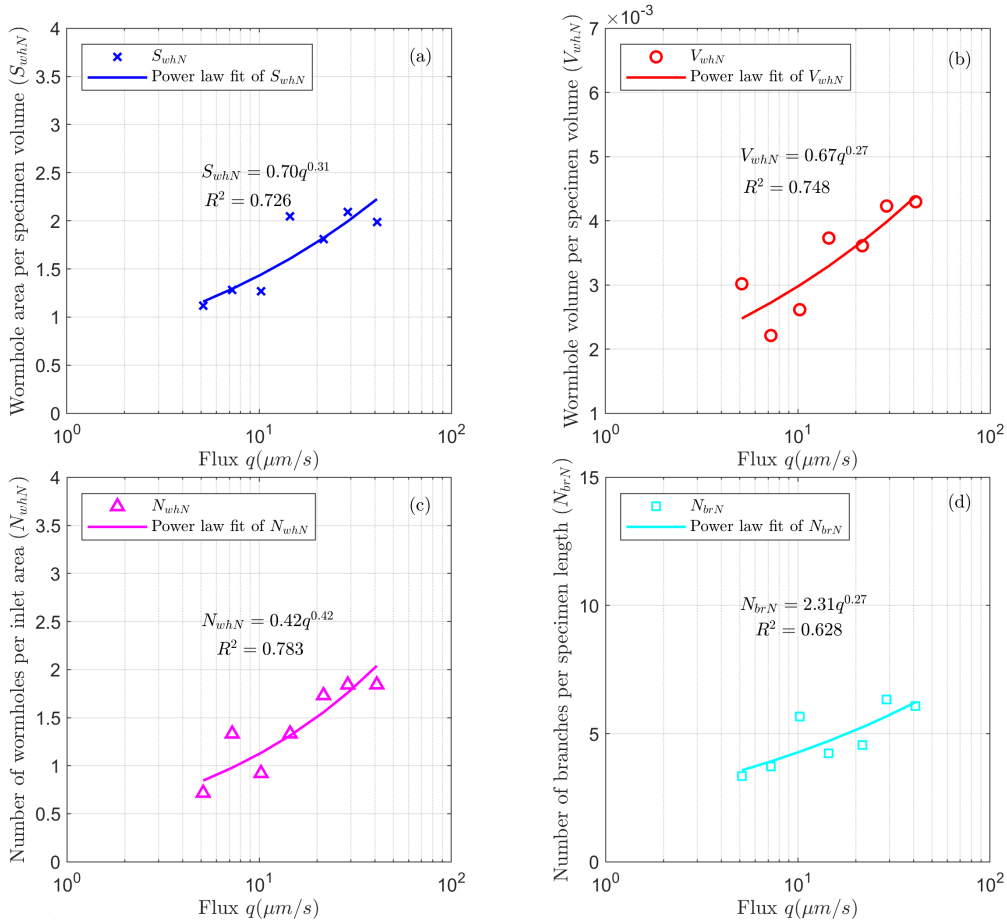

Figure 10. Effect of injection flux on wormhole characteristics. (a) Wormhole surface area per specimen volume (S_{whN} $[m^{-1}]$). (b) Wormhole volume per specimen volume (V_{whN} [1]). (c) The number of wormholes per inlet area (N_{whN} $[cm^{-2}]$). (d) The number of branches per specimen length (N_{brN} $[cm^{-1}]$).

Figure 10(a) shows that higher injection flux (q) tends to result in wormholes with more surface area. Fitting a power law to the relation between S_{whN} and q shows that S_{whN} is proportional to the 0.31 power of q. The wormhole volume per specimen vol-

ume (V_{whN}) is in the range of 2.2−4.3 $\times 10^{-3}$ (Figure 10(b)). This indicates that the wormholes only occupied a small portion of the specimen volume, yet it dramatically increased the permeability from around 20 mD to near infinity. The wormhole volume per specimen volume also shows a positive correlation with the injection flux (q) as shown in Figure 10(b). Fitting a power law to the relation between V_{whN} and q shows that V_{whN} is proportional to the 0.27 power of q

The number of wormholes in each of the seven specimens ranges from 7 to 18. Since the inlet area of the specimens is around 9.8 cm^2, the number of wormholes per inlet area (N_{whN}) ranges from 0.7 to 1.8 (cm^{-2}), as shown in Figure 10(c). A positive correlation is observed between the injection flux and the number of wormholes per inlet area. A power law fit to the relation between N_{whN} and q shows that N_{whN} is proportional to the 0.42 power of q.

The number of branches on the major wormhole ranges from 28 to 53 among the seven specimens. Since the specimen length is around 8.4 cm, the number of branches per specimen length (N_{brN}) range from 3.3 to 6.3 (cm^{-1}), as shown in Figure 10(d). Again, higher injection flux tends to result in more branches. A power law equation is used to fit N_{brN} as a function of the injection flux q. A power law fit between N_{brN} and q shows that N_{whN} is proportional to the 0.27 power of q.

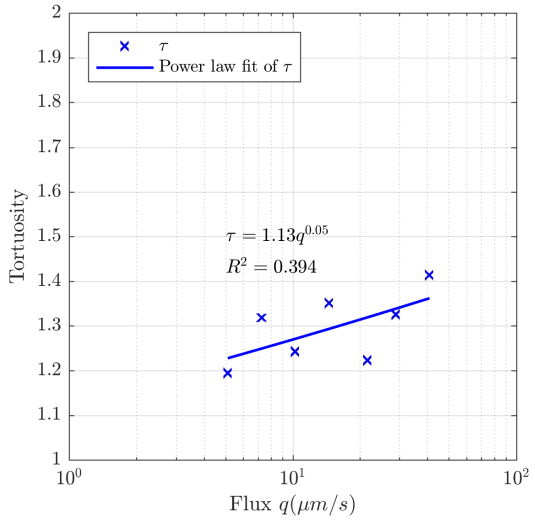

Figure 11. Tortuosity of the major wormholes.

The tortuosity of the major wormhole (τ) ranges from 1.2 to 1.4 among the seven specimens. This shows that the major wormhole, through which most of the injected fluid flows, is slightly longer than the specimen. The tortuosity has a small dependence on the injection flux: the higher flow rates result in higher tortuosity (τ), as shown in Figure 11

In sum, the 3D topological and morphological algorithms provided parameters to quantify the complexity of the wormholes resulting from different flow rates, showing that higher flow rates indeed led to more complex wormhole geometry. Since the wormholes are the results of dissolution heterogeneity in the porous rock matrix, the wormhole geometry can also be used to study the dissolution in the porous rock matrix. The higher number of wormholes and branches resulting from higher injection flux indicate that the dissolution occurs more uniformly in the pore space. This higher number of wormholes and branches in turn more uniformly spread the flow and dissolution in the porous rock matrix before breakthrough of the wormholes. This concept is used in the continuum model to simulate dissolution in porous media in the parallel paper (Li et al., 2019).

4.4 Comparison with Other Tests

The flow and pressure change during the core flood tests were discussed in many experimental studies. This section compares our core flood test results with other test results in the literature (Daccord, Lenormand, & Liétard, 1993; Hoefner & Fogler, 1988). More specifically, the dependence of wormhole growth rate and breakthrough pore volume on the injection flow rate in the core flood tests is compared with those from the literature. Due to the difference in experimental setup and specimen sizes, the parameters from the literature are converted to normalized parameters in this paper to perform proper comparisons.

4.4.1 Wormhole Growth Rate

The conceptual model proposed by Daccord, Lenormand, and Liétard (1993) is used to study the wormhole growth rate (Figure 12). This model divides the specimen with length L_s into the wormhole section with length L_w and the matrix section with the length L_m ($L_s = L_w + L_m$). Similar conceptual models were also proposed by other researchers (Tardy et al., 2007), in which the specimen was subdivided into more sections. These

models do not necessarily describe the microscopic process of wormhole growth; however, they provide a reasonable interpretation of the pressure behavior and wormhole formation.

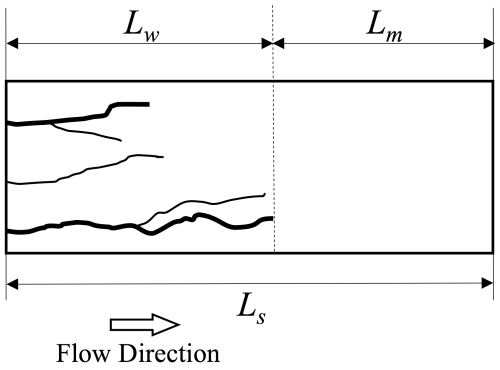

Figure 12. Conceptual model of wormholed specimen proposed by Daccord, Lenormand, and Liétard (1993)

The permeability of the wormhole section is assumed to be infinite, while the permeability of the matrix section is assumed to be the initial permeability of the intact porous medium. With these assumptions, the pressure difference ΔP between the inlet and outlet of the specimen is only associated with the matrix section. If ΔP is normalized to its initial value as $\Delta P_r = \Delta P / \Delta P_0$ and L_w is normalized to the specimen length as $L_{wr} = L_w / L_s$, the following relation can be found:

$$L_{wr} = 1 - L_{mr} = 1 - \Delta P_r. \tag{8}$$

Therefore the pressure data in Figure 7 can be used to calculate the wormhole growth rates for the seven core flood tests. The linearly decreasing part of the relative pressure difference ΔP_r is fitted with a straight line. The result of the test with $Q = 20\ \mu L/s$ is used as an example, as shown in Figure 13(a). The slope of the straight line is the rate of decrease $\frac{\partial \Delta P_r}{\partial V_p}$. Given the relation in Equation (8), $\frac{\partial L_{wr}}{\partial V_p} = -\frac{\partial \Delta P_r}{\partial V_p}$ is the positive value of the slope. $\frac{\partial L_{wr}}{\partial V_p}$ for all the tests are summarized and fitted with a power law, as shown in Figure 13(b). The power law fitting indicates that: $\frac{\partial L_{wr}}{\partial V_p} \propto q^{-0.419}$.

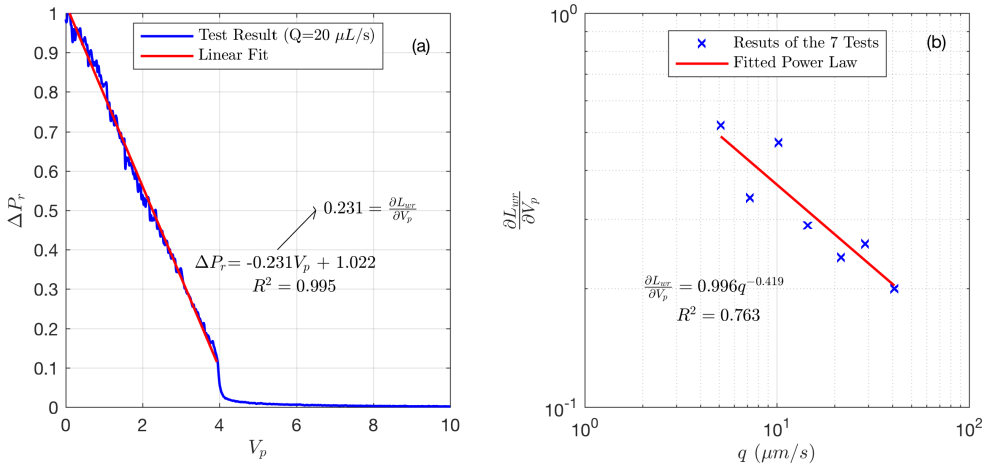

Figure 13. (a) Result of the test with $Q = 20\mu L/s$ is used as an example to show the linear fit of the relative pressure difference as a function of injected pore volume. (b) $\frac{\partial L_{wr}}{\partial V_p}$ of the seven core flood tests is summarized to study the dependence of wormhole growth rate on injection flow rate.

The rate of decrease ($\frac{\partial \Delta P_r}{\partial V_p}$) obtained from the pressure data can be used to calculate the wormhole growth rate, because V_p is a dimensionless linear time coordinate as discussed in Section 4.1. By substituting V_p and L_{wr} with their definitions ($V_p = Q \times t/V_{pore}$ and $L_{wr} = L_w/L_s$, respectively), the wormhole growth rate ($v_E = \frac{\partial L_w}{\partial t}$) can be obtained:

$$v_E = \frac{\partial L_w}{\partial t} = \frac{Q \cdot L_s}{V_{pore}} \cdot \frac{\partial L_{wr}}{\partial V_p}. \tag{9}$$

The term $Q \cdot L_s$ in Equation (9) can also be expressed as $Q \cdot L_s = q \cdot A_s \cdot L_s = q \cdot V_s$, where V_s is the specimen volume. In addition, V_s/V_{pore} is the inverse of porosity $1/n$. The wormhole growth rate (v_E) in Equation (9) can then be further simplified to:

$$v_E = \frac{1}{n} \cdot q \cdot \frac{\partial L_{wr}}{\partial V_p}. \tag{10}$$

Given the power law fitting: $\frac{\partial L_{wr}}{\partial V_p} \propto q^{-0.419}$ (Figure 13), Equation (10) is equivalent to:

$$v_E = \frac{\partial L_w}{\partial t} \propto q \cdot q^{-0.419} \propto q^{0.581}. \tag{11}$$

584 The above discussion shows that based on the conceptual model (Figure 12) the
585 wormholes grow linearly with time (Figure 13(a)). This behavior is consistent with the
586 behavior reported by Daccord et al. (1989). In addition, the wormhole growth rates have
587 a power dependence on the injection flux, with the power of 0.581 (Figure 13(b)). This
588 is close to the value 2/3 reported by Daccord et al. (1989), despite the differences in ex-
589 perimental setup and methods.

590 ***4.4.2 Breakthrough Pore Volume***

591 In the field of petroleum engineering, acid matrix stimulation has been a common
592 method to increase the permeability of reservoirs and enhance oil production. The ef-
593 fectiveness of the acid stimulation often relies on the formation of wormholes that greatly
594 increase the permeability of the matrix without consuming a large quantity of acid. The
595 breakthrough pore volume V_{pbt}, which is the V_p when the wormholes break through, is
596 often used to evaluate the effectiveness of the acid stimulation. Fredd and Fogler (1998)
597 summarized the results of core flood tests with a wide range of rock-fluid systems and
598 fitted an averaging curve to show the relation between the relative breakthrough pore
599 volume V_{pbt}/V_{min} and the inverse Damköhler number $1/D_a$, as shown in Figure 14. V_{min}
600 is the minimum breakthrough pore volume observed in the core flood tests. The Damköhler
601 number D_a in Fredd and Fogler (1998) was defined as the ratio of dissolution rate to ad-
602 vection rate for an idealized cylindrical wormhole. When $1/D_a$ of the rock-fluid system
603 is smaller than 3.4, the resulting dissolution pattern is described as "face dissolution"
604 with no apparent wormholes or one single conical wormhole. When $1/D_a$ is larger than
605 3.4, the resulting dissolution pattern is described as "wormhole dissolution" with one dom-
606 inant wormhole and several others. When $1/D_a$ is much larger than 3.4, the resulting
607 dissolution pattern is described as "uniform dissolution" with many wormholes distributed
608 uniformly in the specimen. In this section, the breakthrough pore volumes V_{pbt} as a func-
609 tion of the inverse Damköhler number $1/D_a$ in our core flood tests were compared with
610 various rock-fluid system summarized by Fredd and Fogler (1998).

611 In our gypsum core flood tests, the idealized wormhole had a length of $85mm$ and
612 a diameter of $2mm$ according to the CT scan analysis Figure 9. The diffusivity of the

calcium ion, $9\times10^{-10}m^2/s$, was used for the diffusivity of the solute. Since the dissolution of gypsum in water is in general transport-controlled (Li & Einstein, 2017), the formulation for transport-controlled dissolution proposed by Fredd and Fogler (1998) was used to calculate the effective dissolution rate constant. The calculated inverse Damköhler numbers $1/D_a$ for our core flood test were in the range from 15 to 70.

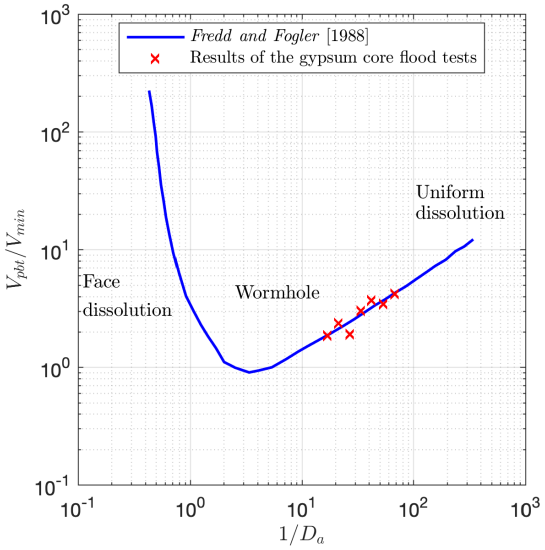

Figure 14. Breakthrough pore volumes as a function of inverse Damköhler number. The gypsum core flood tests show consistent behavior with the various rock-fluid systems summarized by Fredd and Fogler (1998)

Either the pressure difference data (Figure 7(b)) or the effluent concentration data (Figure 7(c)) can be used to find the breakthrough pore volume V_{pbt} in our gypsum core flood tests. Since the minimum breakthrough pore volume V_{min} was not observed in the seven tests, an assumption has to be made for V_{min} to calculate the relative breakthrough pore volume V_{pbt}/V_{min}. With the assumed minimum breakthrough pore volume $V_{min} = 1.2$, the results of the gypsum core flood tests match the summary of Fredd and Fogler (1998) very well, as shown in Figure 14. It should be noted that the assumption of the minimum breakthrough pore volume V_{min} only affects the vertical position of the data points for the gypsum core flood tests. Even without the assumption of V_{min}, the slope of the data points would still match the slope in Fredd and Fogler (1998).

4.4.3 Summary of Flow and Pressure Analyses

The flow and pressure analyses above show that our core flood tests are consistent with the core flood tests in a wide range of rock-fluid systems reported in the literature (Daccord et al., 1989; Fredd & Fogler, 1998). The wormhole growth rate of our core flood test is proportional to the 0.581 power of the injection flux (see Equation (11)). This is close to the 2/3 power reported by Daccord et al. (1989). In addition, the breakthrough pore volumes of our core flood tests have a dependence on the inverse Damköhler number, which is consistent with the result summarized by Fredd and Fogler (1998) for various rock-fluid systems.

4.5 Mass and Volume Change

The change of mass and volume during dissolution were studied by (a), measuring the mass of the specimen before and after the test; (b), integrating the effluent concentration with the volume to calculate the dissolved mass; and (c) measuring the wormhole volume using CT scan. The dissolved mass measured using the three methods is much smaller than the mass of the specimen, which results in a limited accuracy of measurement. In addition, the effluent concentration measurement using ECMS in the initial transient state is affected by dissolved air; therefore, the study of mass and volume change is only qualitative.

The dissolved mass measured using method (a) is around 1 g. The dissolved mass calculated using method (b), by integrating the effluent concentration over the injected volume, is also around 1 g. The wormhole volume measured using the CT scan (method (c)) is around 0.3 cm^3, which corresponds to the mass of 0.25 g. The difference of 0.75 g dissolved mass should come from the dissolution in the matrix or wormholes shorter than 5 mm in length, which were not accounted for by wormhole reconstruction. The specimen has a total mass of around 100 g, so the dissolved material from the matrix is only a small part ($< 1\%$) of the specimen. However, this small part changed the permeability of the specimen from around 24 mD to almost infinity. This again shows the effectiveness of wormhole formation in increasing the permeability of the material without dissolving a large amount of material.

5 Summary and Conclusions

This paper presented the advanced experimental methods and data analyses algorithms to study the reactive transport processes in soluble porous rocks. More specifically, an effluent chemistry monitoring system (ECMS) was designed and integrated into the triaxial system to provide continuous concentration measurements of the effluent. 3D topological and morphological algorithms were developed to quantitatively analyze the wormhole geometry based on the CT data. These methods provided new insights into the effect of flow rate on the dissolution of the gypsum rock matrix and the formation of wormholes.

The continuous effluent concentration data from the ECMS provided useful information on the overall dissolution rate and the evolution of the rock-fluid system. With a constant flow rate, the overall dissolution rate is higher before the wormhole breakthrough than after the wormhole breakthrough. The wormhole breakthrough is accompanied by a sudden effluent concentration drop, as also reported in the literature (Hoefner & Fogler, 1988). This indicated that the wormhole breakthrough changed the overall dissolution kinetics in the rock-fluid system. The effluent concentration data are analyzed in detail to study the evolution of dissolution kinetics and its physical implications for the rock-fluid system in the parallel paper.

CT scanning was used to observe the pore space and wormholes before and after the core flood tests. 3D topological and morphological algorithms were developed to provide quantitative descriptions of the wormhole geometry, such as the wormhole surface area, the wormhole volume, the number of wormholes, the number of branches. These parameters were used to quantitatively study the effect of flow rate on the wormhole geometries. The wormhole geometry analyses showed that higher flow rates result in larger wormhole surface area and volume, more wormholes, more branches and slightly higher wormhole tortuosity. Since the wormholes are the result of flow and dissolution heterogeneities in the porous matrix, the wormhole geometries can be used to evaluate the dissolution of the matrix under different flow rates. In the parallel paper (Li et al., 2019), the quantitative wormhole geometry analyses are used when modeling the dissolution in the matrix.

The flow and pressure data were analyzed to study the rate of wormhole growth and breakthrough pore volume as functions of the injection flow rate (or flux) in the gypsum-

water system during the core flood tests. During each core flood tests, the wormholes developed with a constant rate of growth. The wormhole growth rates of the core flood tests have a power dependence on the injection flux, with a power of 0.581. This result is close to the observation by Daccord, Lenormand, and Liétard (1993), in which the power was 2/3. The analyses also showed that higher injection flow rates required more pore volumes to breakthrough the specimen. The dependence of breakthrough pore volume on the inverse Damköhler number (a function of flow rate) is consistent with the relation summarized by Fredd and Fogler (1998) for various rock-fluid systems. The study of the wormhole growth and breakthrough can be used to predict the length of the wormhole section and wormhole breakthrough for laboratory-scale models. It is also possible to use these relations at the field scale with proper upscaling and calibration.

The use of laboratory cast gypsum specimens facilitated the systematic study of the effect of flow rate on the dissolution of the gypsum rock matrix and the formation of wormholes. Given the consistent properties of the gypsum specimen and its relatively simple reaction with water, this experimental study can be used as a reference for comparison to more complex rock-water systems, for example, a calcite-HCl system. The innovations of the experimental methods, especially the ECMS, can also be used to study flow and dissolution in other rocks that have relatively simple chemical composition.

Appendix A Acid capacity number (N_{ac}) for the gypsum-water system

By assuming that the total volume of the matrix is V_t, the initial pore volume can be expressed as:

$$\phi_0 V_t; \tag{A1}$$

where ϕ_0 is the initial porosity. The mass of solid that can be dissolved by the volume $\phi_0 V_t$ pore fluid is:

$$\phi_0 V_t C_{eq} \tag{A2}$$

where $C_{eq}[M/L^3]$ is the equilibrium concentration of the gypsum in water. The mass of the matrix is:

$$(1-\phi_0)V_t \cdot \rho_s; \tag{A3}$$

where ρ_s is the density of the mineral. The above derivation yields the acid capacity number:

$$N_{ac} = \frac{\phi_0 C_{eq}}{(1-\phi_0)\rho_s}. \tag{A4}$$

Acknowledgments

This work was partially funded by the Abu Dhabi National Oil Company and the Cooperative Agreement between the Masdar Institute of Science and Technology (Masdar Institute), Abu Dhabi, UAE and the Massachusetts Institute of Technology (MIT), Cambridge, MA, USA - Reference 02/MI/MIT/CP/11/07633/GEN/G/00. The authors also acknowledge the help in designing and fabricating the ECMS from Stephen W. Rudolph in the Department of Civil and Environmental Engineering at MIT. The authors also thank their colleagues Rafael Villamor Lora and Hao Kang for their help in updating and servicing the triaxial system. The experimental data supporting this work are publicly available online (http://dx.doi.org/10.17632/ywsx639ybw.1).

References

Abdulhadi, N. O., Germaine, J. T., & Whittle, A. J. (2011). Thick-walled cylinder testing of clays for the study of wellbore instability. *Geotechnical Testing Journal*, *34*(6), 746–754.

Adams, A. L., Nordquist, T. J., Germaine, J. T., & Flemings, P. B. (2016). Permeability anisotropy and resistivity anisotropy of mechanically compressed mudrocks. *Canadian Geotechnical Journal*, *53*(9), 1474–1482.

Al-Khulaifi, Y., Lin, Q., Blunt, M. J., & Bijeljic, B. (2018). Reservoir-condition pore-scale imaging of dolomite reaction with supercritical CO_2 acidified brine: Effect of pore-structure on reaction rate using velocity distribution analysis. *International Journal of Greenhouse Gas Control*, *68*, 99–111.

Andersen, G. R. (1991). *Physical mechanisms controlling the strength and deformation behavior of frozen sand* (Unpublished doctoral dissertation). Massachusetts Institute of Technology.

Budek, A., & Szymczak, P. (2012). Network models of dissolution of porous media. *Physical Review E*, *86*(5), 056318.

Cai, Z., Wen, H., Komarneni, S., & Li, L. (2018). Mineralogy controls on reactive transport of marcellus shale waters. *Science of The Total Environment*, *630*, 1573–1582.

Daccord, G. (1987). Chemical dissolution of a porous medium by a reactive fluid. *Physical review letters*, *58*(5), 479.

Daccord, G., & Lenormand, R. (1987). Fractal patterns from chemical dissolution. *Nature*, *325*(6099), 41–43.

Daccord, G., Lenormand, R., & Liétard, O. (1993). Chemical dissolution of a porous medium by a reactive fluid –i. model for the "wormholing" phenomenon. *Chemical Engineering Science*, *48*(1), 169–178.

Daccord, G., Liétard, O., & Lenormand, R. (1993). Chemical dissolution of a porous medium by a reactive fluid –ii. convection vs reaction, behavior diagram. *Chemical engineering science*, *48*(1), 179–186.

Daccord, G., Touboul, E., & Lenormand, R. (1989). Carbonate acidizing: toward a quantitative model of the wormholing phenomenon. *SPE production engineering*, *4*(01), 63–68.

Deng, H., Fitts, J. P., Crandall, D., McIntyre, D., & Peters, C. A. (2015). Alterations of fractures in carbonate rocks by co2-acidified brines. *Environmental science & technology*, *49*(16), 10226–10234.

Deng, H., Fitts, J. P., & Peters, C. A. (2016). Quantifying fracture geometry with x-ray tomography: Technique of iterative local thresholding (tilt) for 3d image segmentation. *Computational Geosciences*, *20*(1), 231–244.

Deng, H., Voltolini, M., Molins, S., Steefel, C., DePaolo, D., Ajo-Franklin, J., & Yang, L. (2017). Alteration and erosion of rock matrix bordering a carbonate-rich shale fracture. *Environmental science & technology*, *51*(15), 8861–8868.

Einstein, H., Hirschfeld, R., Nelson, R., & Bruhn, R. (1969). Model studies of jointed-rock behavior. In *The 11th us symposium on rock mechanics (usrms).*

El-Maghraby, R. M., & Blunt, M. J. (2012). Residual CO_2 trapping in indiana limestone. *Environmental science & technology*, *47*(1), 227–233.

Fredd, C. N., & Fogler, H. S. (1998). Influence of transport and reaction on wormhole formation in porous media. *AIChE journal*, *44*(9), 1933–1949.

Ghommem, M., Zhao, W., Dyer, S., Qiu, X., & Brady, D. (2015). Carbonate acidizing: modeling, analysis, and characterization of wormhole formation and propagation. *Journal of Petroleum Science and Engineering*, *131*, 18–33.

Giesche, H. (2006). Mercury porosimetry: a general (practical) overview. *Particle & particle systems characterization*, *23*(1), 9–19.

Golfier, F., ZARCONE, C., Bazin, B., Lenormand, R., Lasseux, D., & QUINTARD, M. (2002). On the ability of a darcy-scale model to capture wormhole formation during the dissolution of a porous medium. *Journal of fluid Mechanics*, *457*, 213–254.

Gomaa, A. M., & Nasr-El-Din, H. A. (2010). New insights into the viscosity of polymer-based in-situ-gelled acids. *SPE Production & Operations*, *25*(03), 367–375.

Gouze, P., Noiriel, C., Bruderer, C., Loggia, D., & Leprovost, R. (2003). X-ray tomography characterization of fracture surfaces during dissolution. *Geophysical Research Letters*, *30*(5).

Hao, Y., Smith, M., Sholokhova, Y., & Carroll, S. (2013). CO_2-induced dissolution of low permeability carbonates. part ii: Numerical modeling of experiments. *Advances in water resources*, *62*, 388–408.

Hoefner, M., & Fogler, H. S. (1988). Pore evolution and channel formation during flow and reaction in porous media. *AIChE Journal*, *34*(1), 45–54.

James, A., & Lupton, A. (1978). Gypsum and anhydrite in foundations of hydraulic structures. *Geotechnique*, *28*(3), 249–272.

Jeschke, A. A., Vosbeck, K., & Dreybrodt, W. (2001). Surface controlled dissolution rates of gypsum in aqueous solutions exhibit nonlinear dissolution kinetics. *Geochimica et Cosmochimica Acta*, *65*(1), 27–34.

Johnson, K. S. (2008). Gypsum-karst problems in constructing dams in the usa. *Environmental geology*, *53*(5), 945–950.

Li, W., & Einstein, H. H. (2017). Theoretical and numerical investigation of the cavity evolution in gypsum rock. *Water Resources Research*, *53*(11), 9988–10001.

Li, W., Einstein, H. H., & Germaine, J. T. (2019). An experimental study of matrix dissolution and wormhole formation using gypsum core flood tests. part ii dissolution kinetics and modeling. *Journal of Geophysical Research: Solid Earth*, *xx*, xx–xx.

Lin, Q., Al-Khulaifi, Y., Blunt, M. J., & Bijeljic, B. (2016). Quantification of sub-resolution porosity in carbonate rocks by applying high-salinity contrast brine using x-ray microtomography differential imaging. *Advances in water resources*, *96*, 306–322.

Menke, H., Andrew, M., Blunt, M., & Bijeljic, B. (2016). Reservoir condition imaging of reactive transport in heterogeneous carbonates using fast synchrotron tomographyeffect of initial pore structure and flow conditions. *Chemical Geology*, *428*, 15–26.

Menke, H., Reynolds, C., Andrew, M., Nunes, J. P., Bijeljic, B., & Blunt, M. (2018). 4d multi-scale imaging of reactive flow in carbonates: Assessing the impact of heterogeneity on dissolution regimes using streamlines at multiple length scales. *Chemical Geology*, *481*, 27–37.

Mohamed, I. M., He, J., & Nasr-El-Din, H. A. (2013). Experimental analysis of co2 injection on permeability of vuggy carbonate aquifers. *Journal of Energy Resources Technology*, *135*(1), 013301.

No. 1 moulding plasters (Tech. Rep. No. SDS NO. 52000000006). (2017, 3). 550 West Adams Street, Chicago, Illinois, 60661: United States Gypsum Company. (Version #: 3)

Noiriel, C. (2015). Resolving time-dependent evolution of pore-scale structure, permeability and reactivity using x-ray microtomography. *Reviews in Mineralogy and Geochemistry*, *80*(1), 247–285.

Noiriel, C., Bernard, D., Gouze, P., & Thibault, X. (2005). Hydraulic properties and microgeometry evolution accompanying limestone dissolution by acidic water. *Oil & gas science and technology*, *60*(1), 177–192.

Noiriel, C., & Daval, D. (2017). Pore-scale geochemical reactivity associated with CO_2 storage: New frontiers at the fluid–solid interface. *Accounts of chemical research*, *50*(4), 759–768.

Noiriel, C., & Deng, H. (2018). Evolution of planar fractures in limestone: The role of flow rate, mineral heterogeneity and local transport processes. *Chemical Geology*, *497*, 100–114.

Noiriel, C., Gouze, P., & Bernard, D. (2004). Investigation of porosity and permeability effects from microstructure changes during limestone dissolution. *Geophysical research letters*, *31*(24).

Noiriel, C., Luquot, L., Madé, B., Raimbault, L., Gouze, P., & Van Der Lee, J. (2009). Changes in reactive surface area during limestone dissolution: An experimental and modelling study. *Chemical Geology*, *265*(1-2), 160–170.

Noiriel, C., Steefel, C. I., Yang, L., & Bernard, D. (2016). Effects of pore-scale precipitation on permeability and flow. *Advances in water resources*, *95*, 125–137.

Ramsay, W. B. (1996). *A modified triaxial permeameter for physical characterization of parameters affecting contaminant transport through wetland deposits* (Unpublished doctoral dissertation). Massachusetts Institute of Technology.

Reynolds, C., Blunt, M., & Krevor, S. (2014). Impact of reservoir conditions on co_2-brine relative permeability in sandstones. *Energy Procedia*, *63*, 5577–5585.

Russ, J. C. (2016). *The image processing handbook*. CRC press.

Sayed, M. A. I., Zakaria, A. S. E. D., Nasr-El-Din, H. A., Holt, S. P., & Almalki, H. (2012). Core flood study of a new emulsified acid with reservoir cores. In *Spe international production and operations conference & exhibition.*

Serafeimidis, K., & Anagnostou, G. (2013). On the time-development of sulphate hydration in anhydritic swelling rocks. *Rock mechanics and rock engineering*, *46*(3), 619–634.

Sheahan, T. C., & Germaine, J. T. (1992). Computer automation of conventional triaxial equipment. *Geotechnical Testing Journal*, *15*(4), 311–322.

Smith, M. M., Hao, Y., & Carroll, S. (2017). Development and calibration of a reactive transport model for carbonate reservoir porosity and permeability changes based on CO_2 core-flood experiments. *International Journal of Greenhouse Gas Control*, *57*, 73–88.

Smith, M. M., Hao, Y., Mason, H. E., & Carroll, S. A. (2014). Experiments and modeling of variably permeable carbonate reservoir samples in contact with co2-acidified brines. *Energy Procedia*, *63*(C).

Smith, M. M., Sholokhova, Y., Hao, Y., & Carroll, S. A. (2013). CO_2-induced dissolution of low permeability carbonates. part i: Characterization and experiments. *Advances in Water Resources*, *62*, 370–387.

Tardy, P. M. J., Lecerf, B., & Christanti, Y. (2007). An experimentally validated wormhole model for self-diverting and conventional acids in carbonate rocks under radial flow conditions. In *European formation damage conference.*

Taylor, K., & Nasr-El-Din, H. (2002). Coreflood evaluation of in-situ gelled acids. In *International symposium and exhibition on formation damage control.*

Wang, H., Bernabé, Y., Mok, U., & Evans, B. (2016). Localized reactive flow in carbonate rocks: Core-flood experiments and network simulations. *Journal of Geophysical Research: Solid Earth*, *121*(11), 7965–7983.

Wang, Y., Hill, A., & Schechter, R. (1993). The optimum injection rate for matrix acidizing of carbonate formations. In *Spe annual technical conference and exhibition.*

Yang, Y., Hakim, S. S., Bruns, S., Rogowska, M., Boehnert, S., Hammel, J., ... Sørensen, H. O. (2018). Direct observation of coupled geochemical and geomechanical impacts on chalk microstructure evolution under elevated co2 pressure. *ACS Earth and Space Chemistry*, *2*(6), 618–633.

Figure 1.

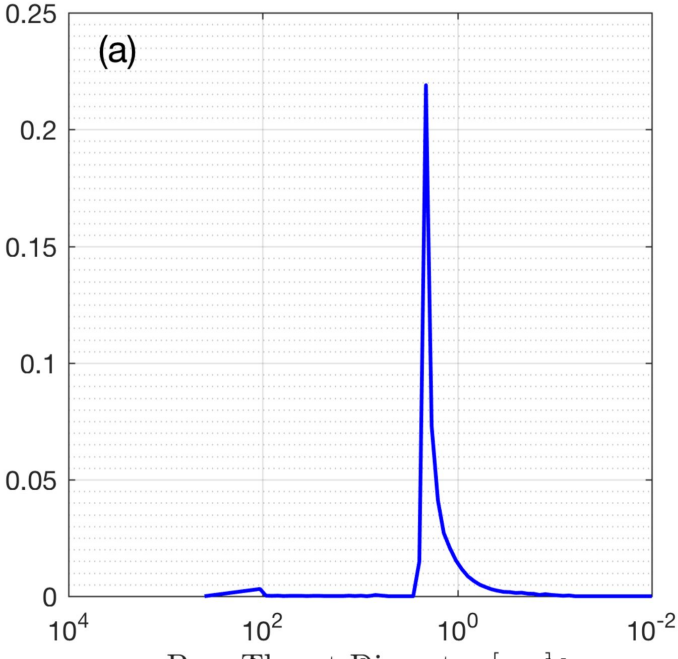

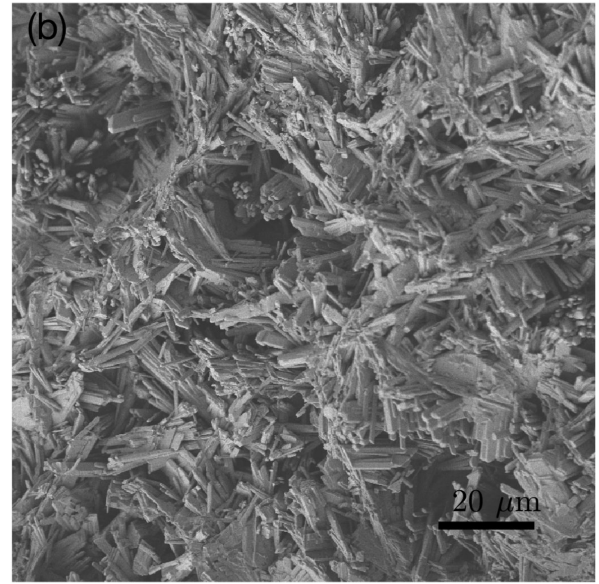

Figure 2.

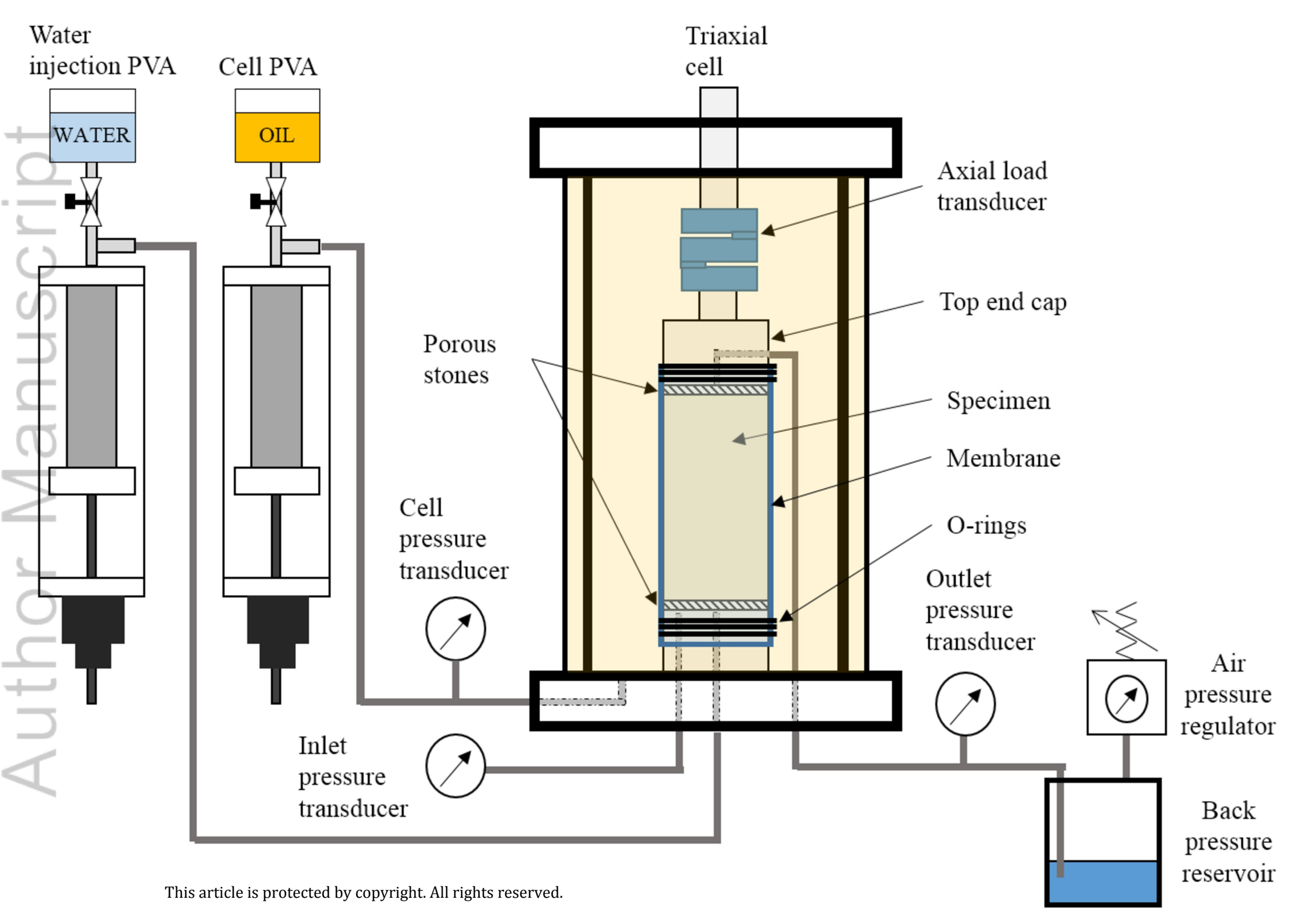

Figure 3.

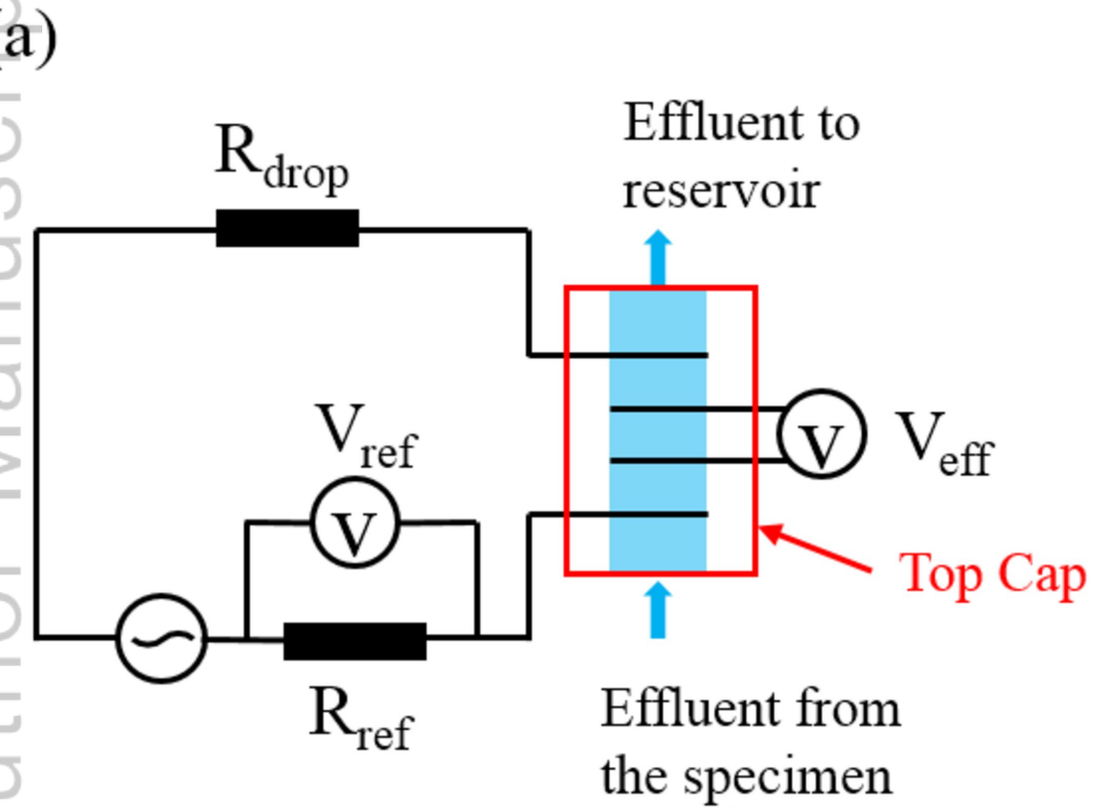

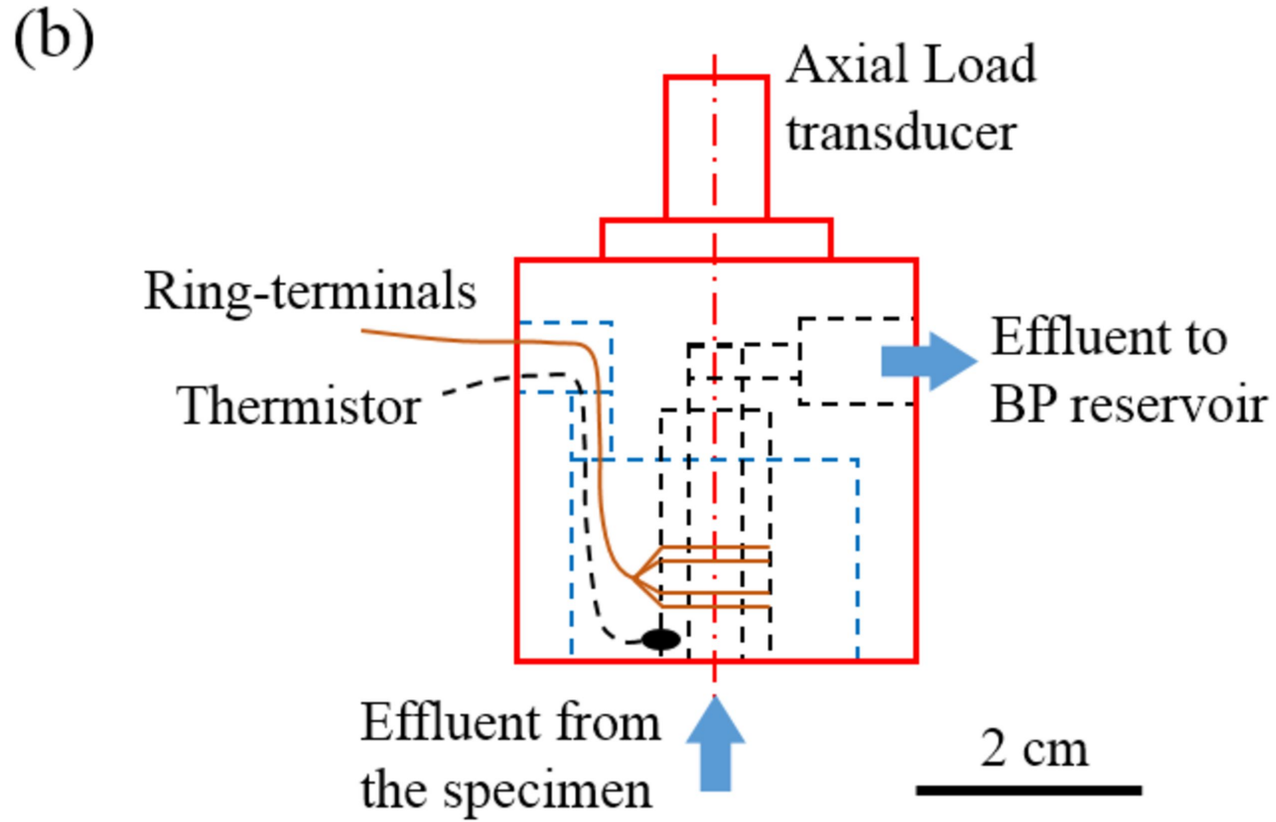

Figure 4.

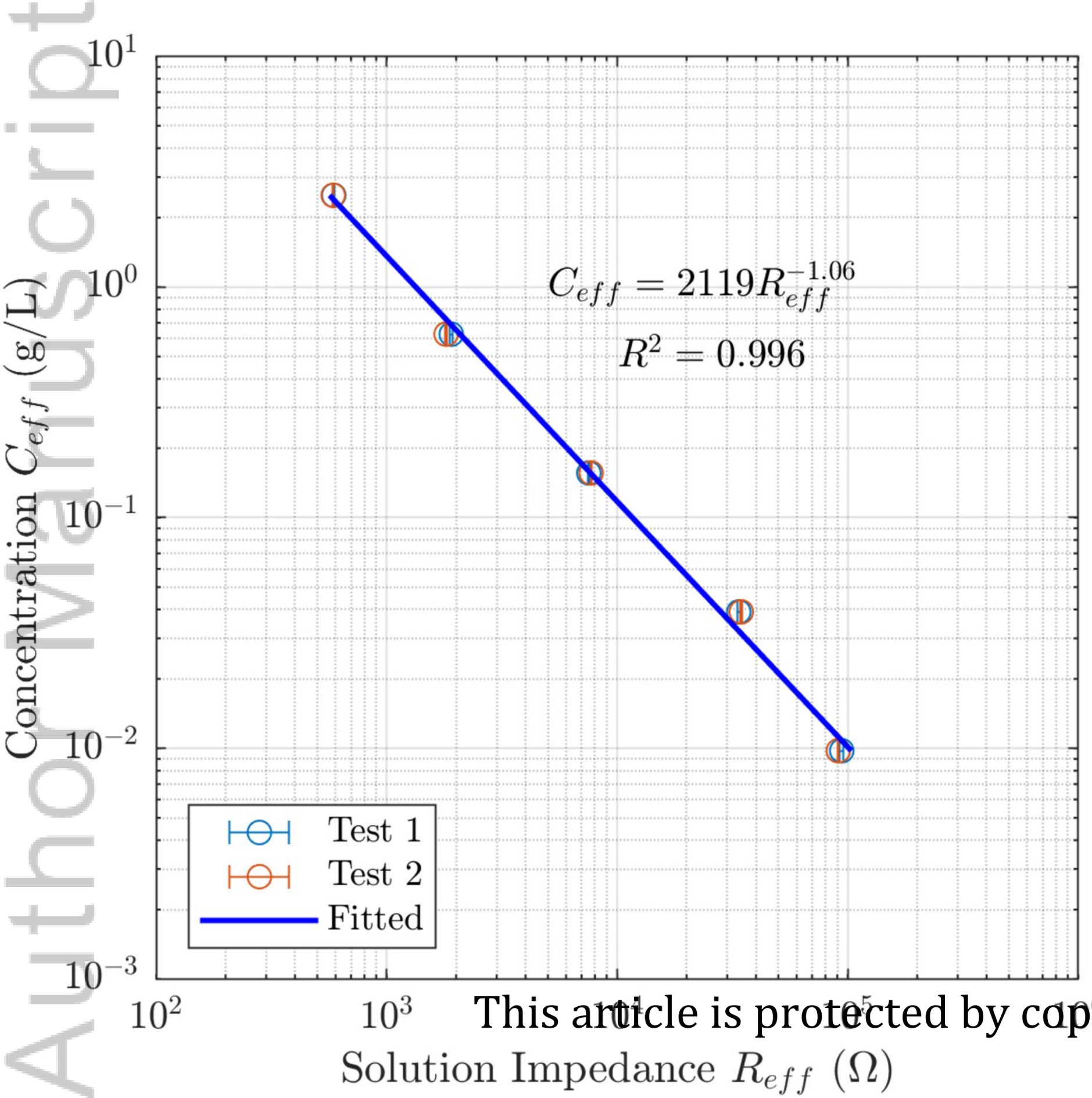

Figure 5.

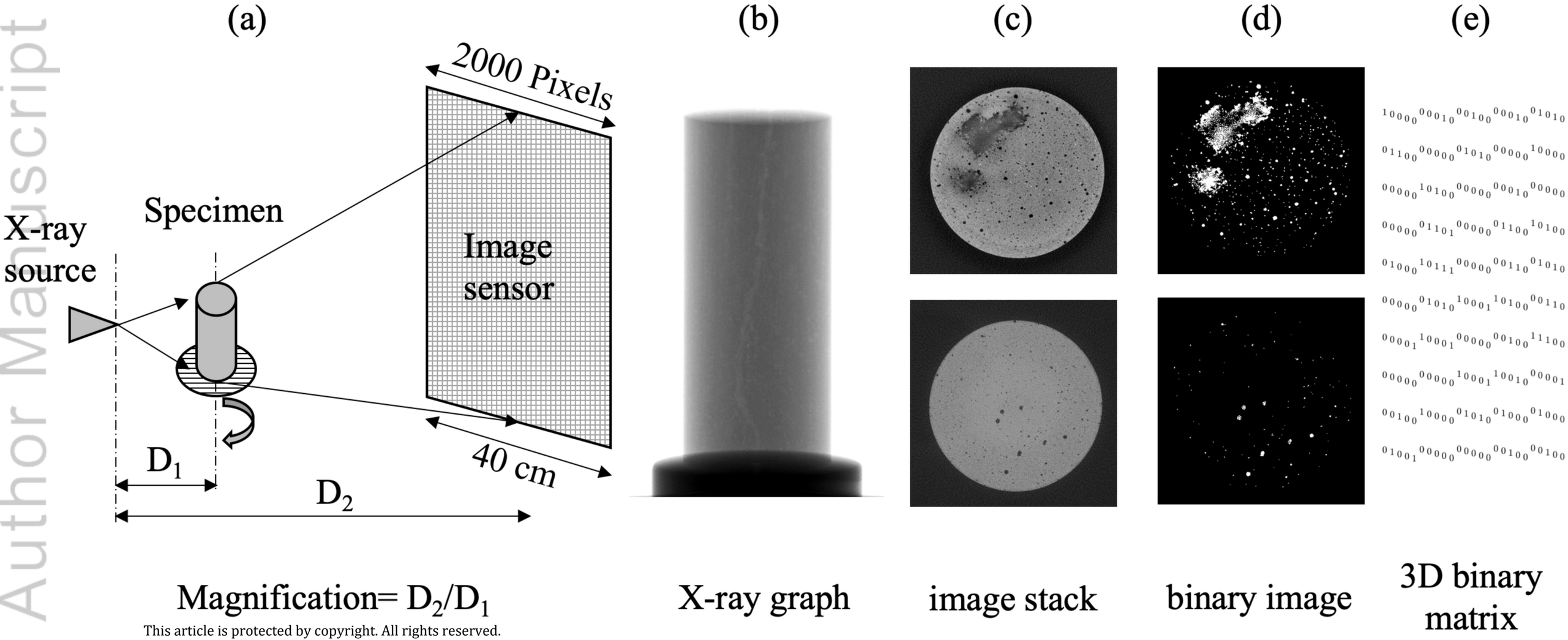

Figure 6.

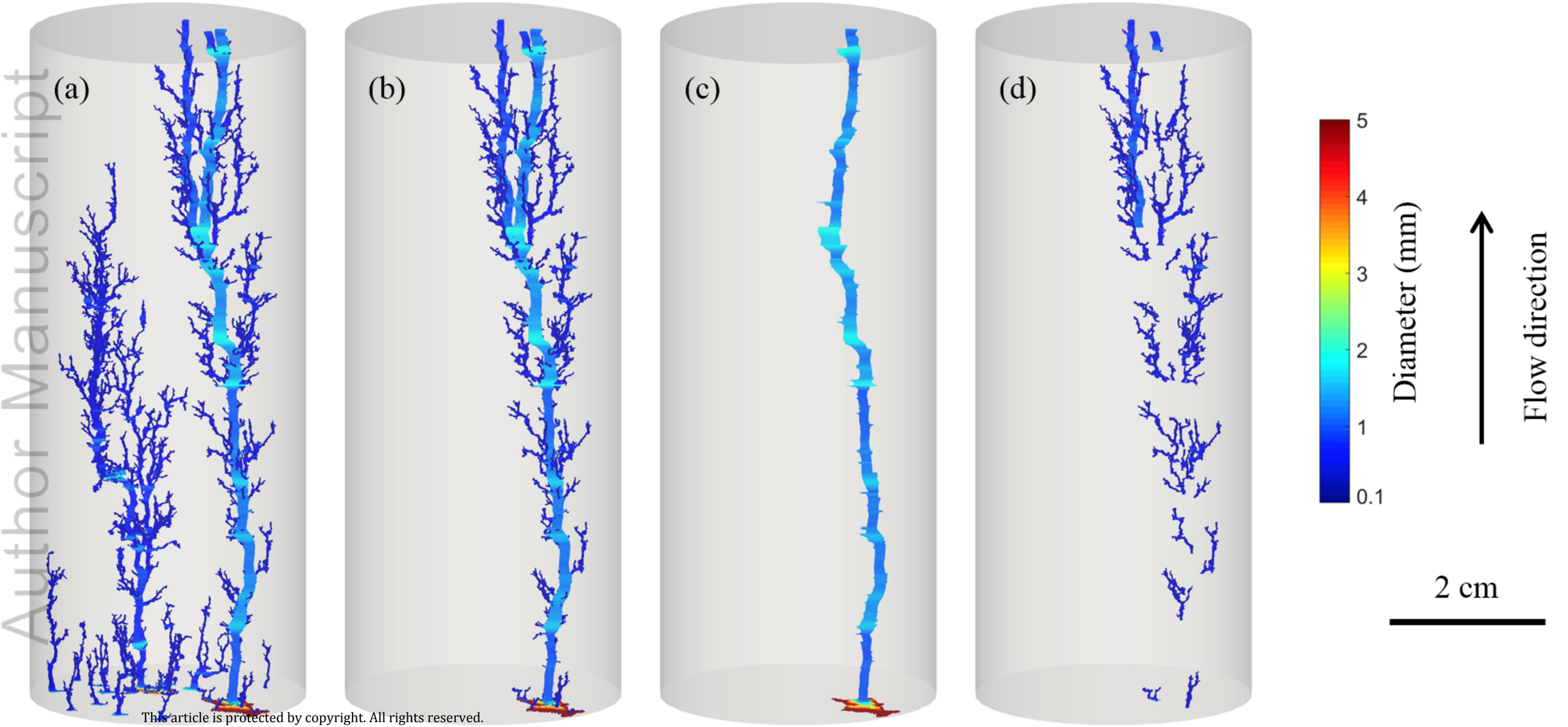

Figure 7.

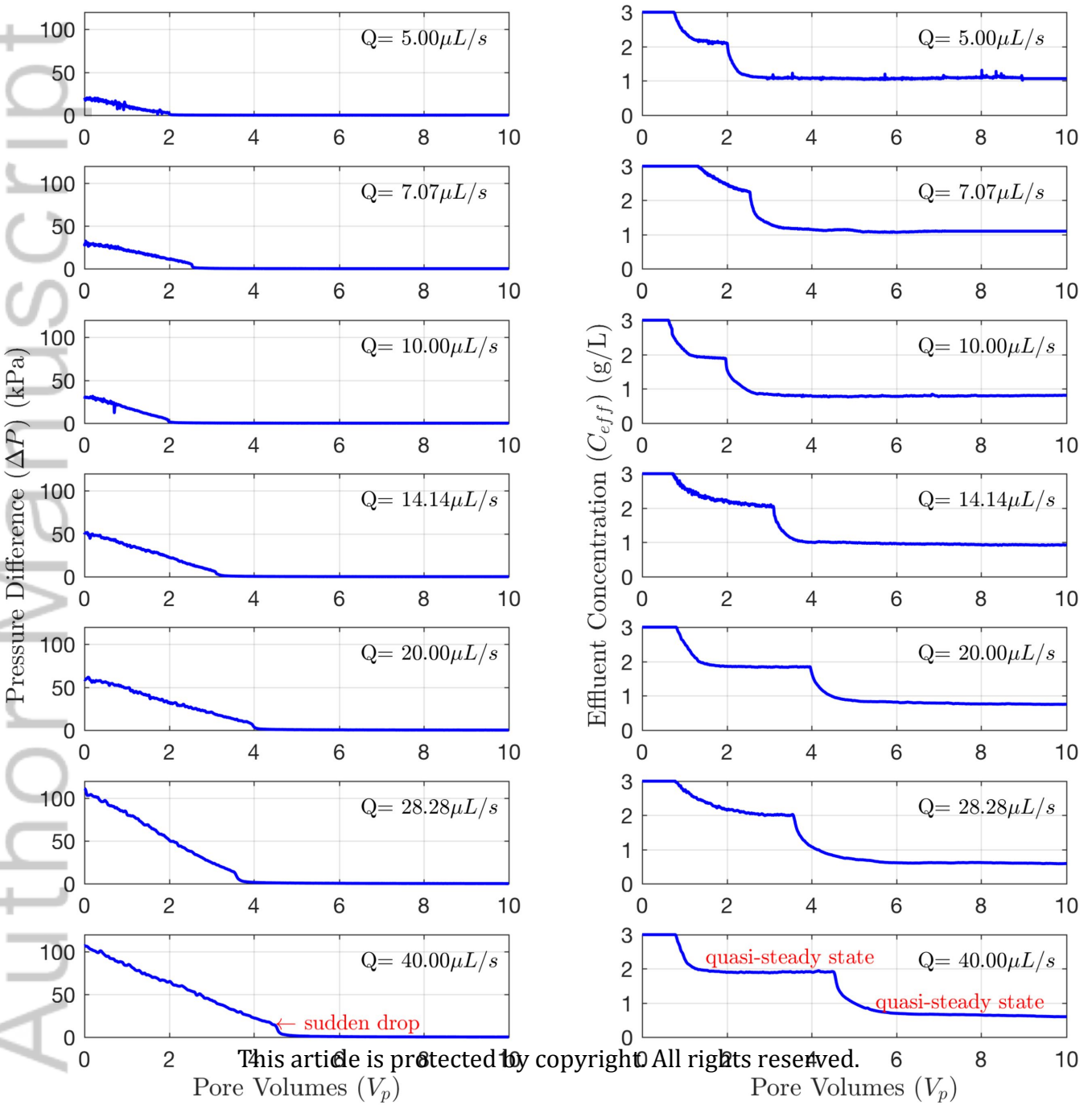

Figure 8.

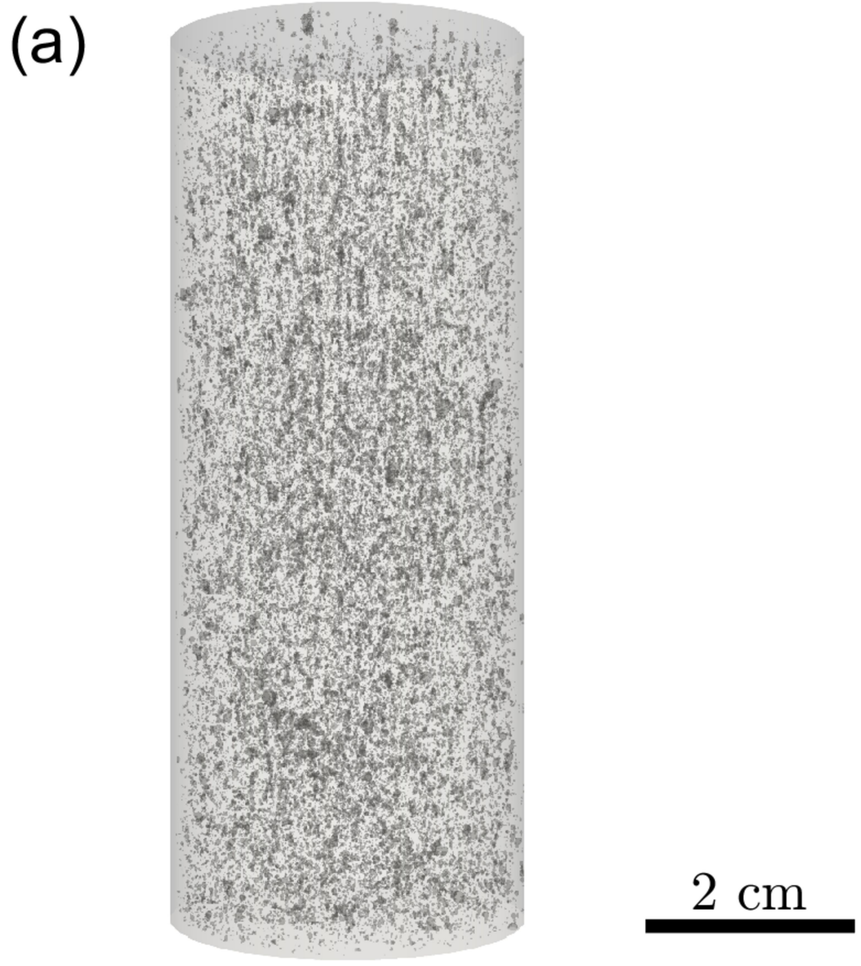

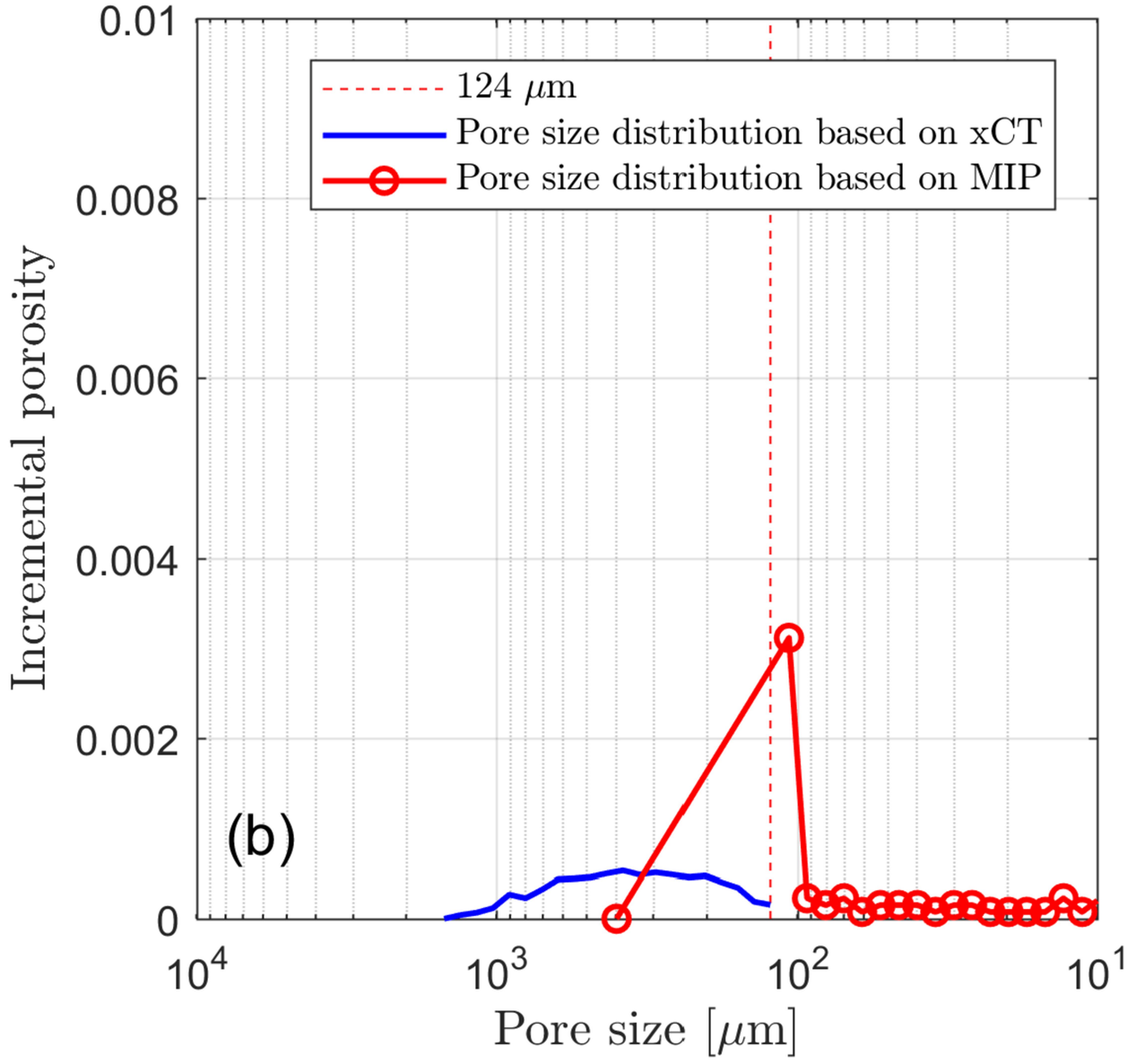

Figure 9.

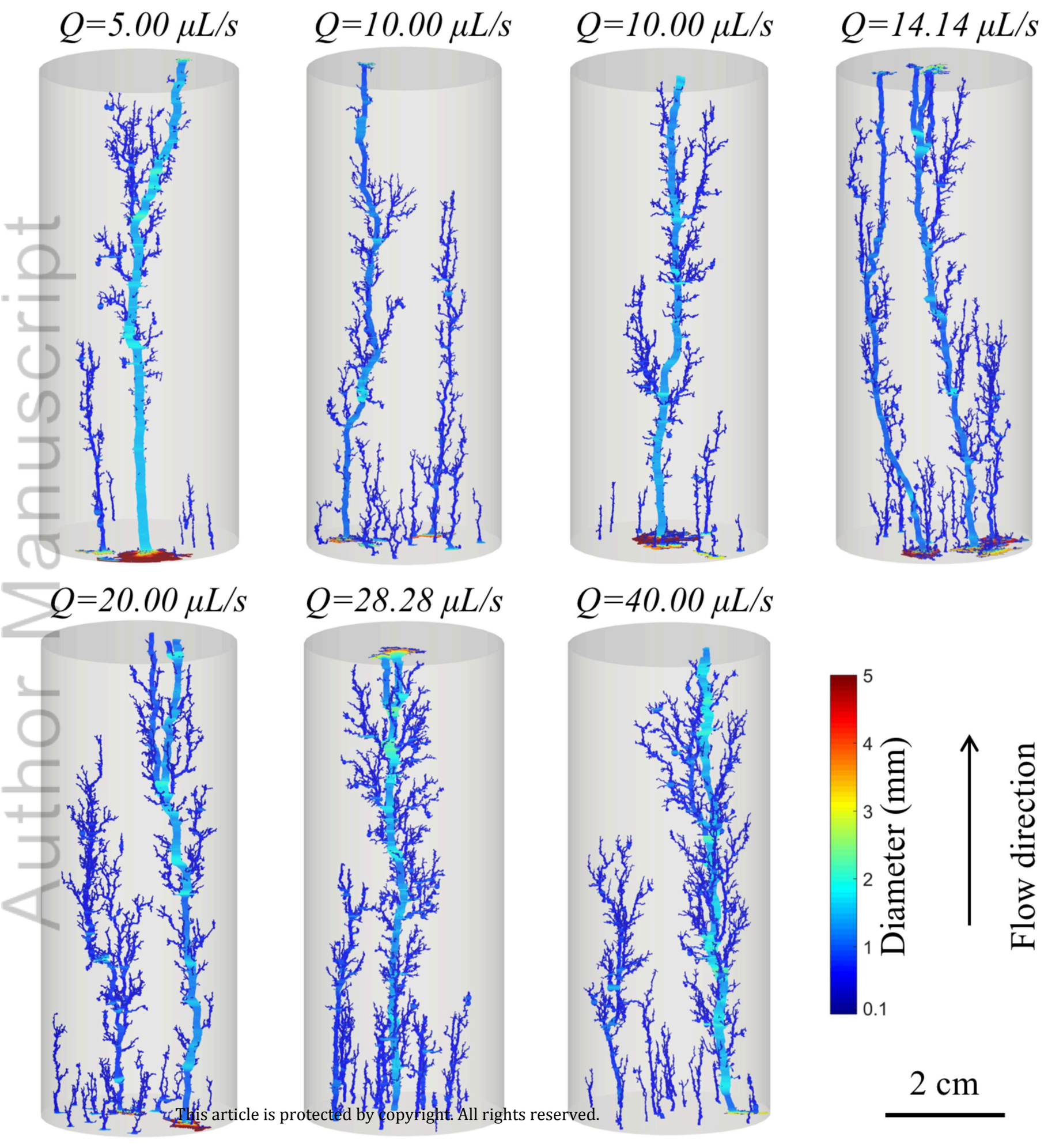

Figure 10.

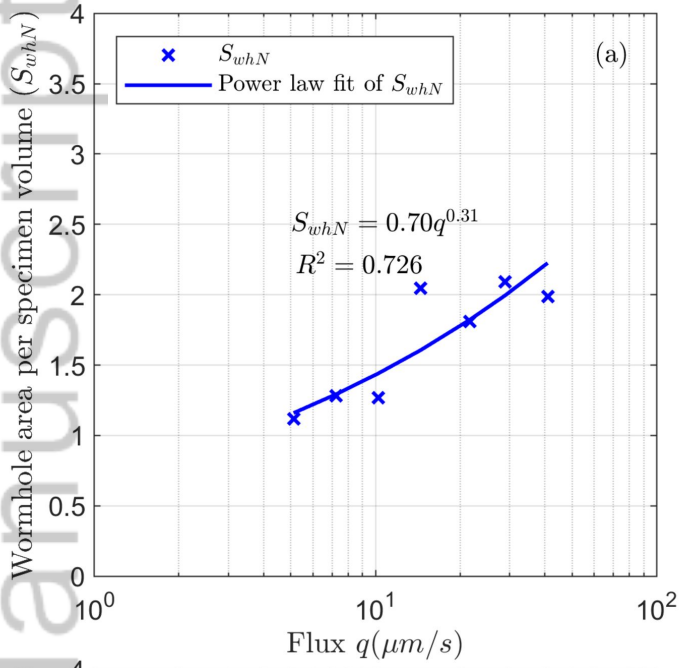

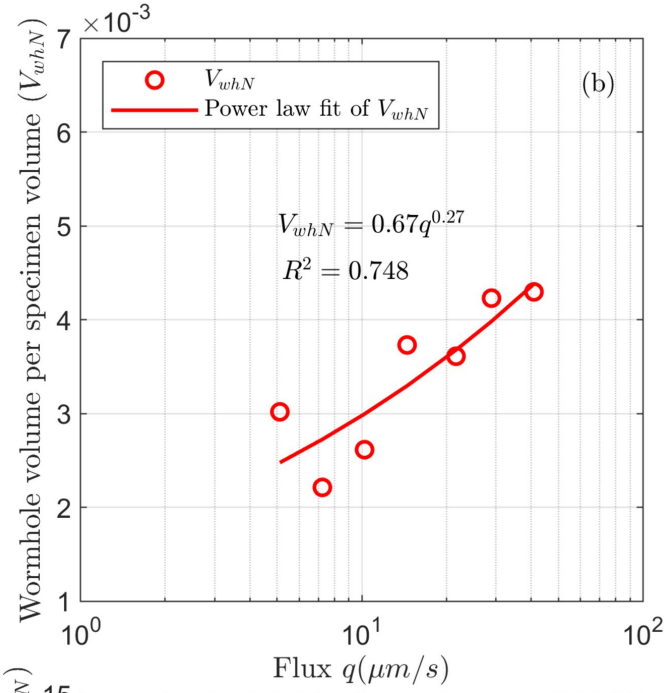

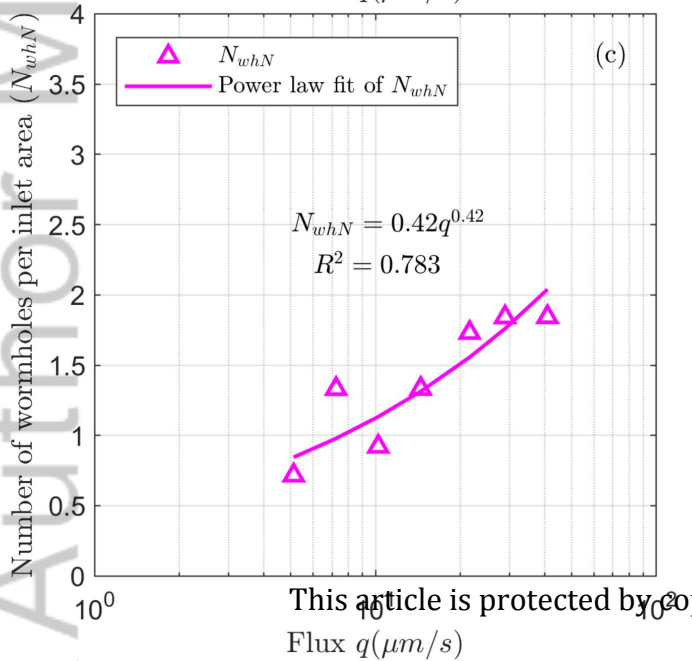

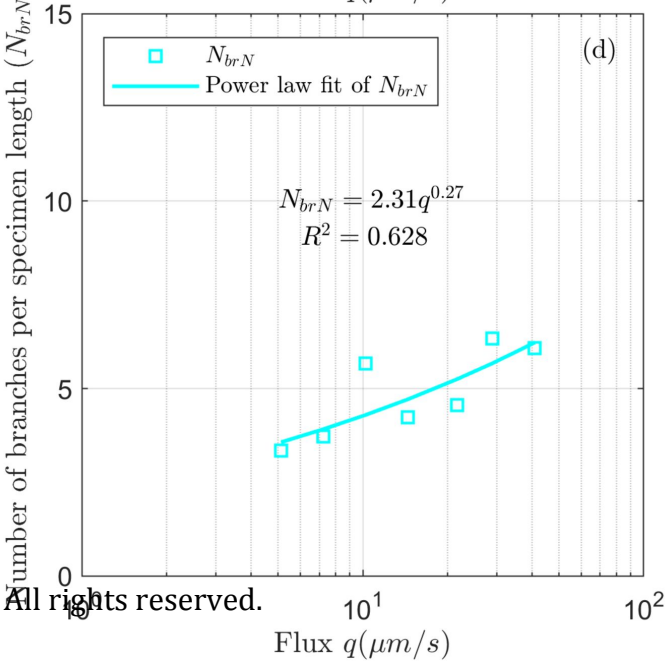

Figure 11.

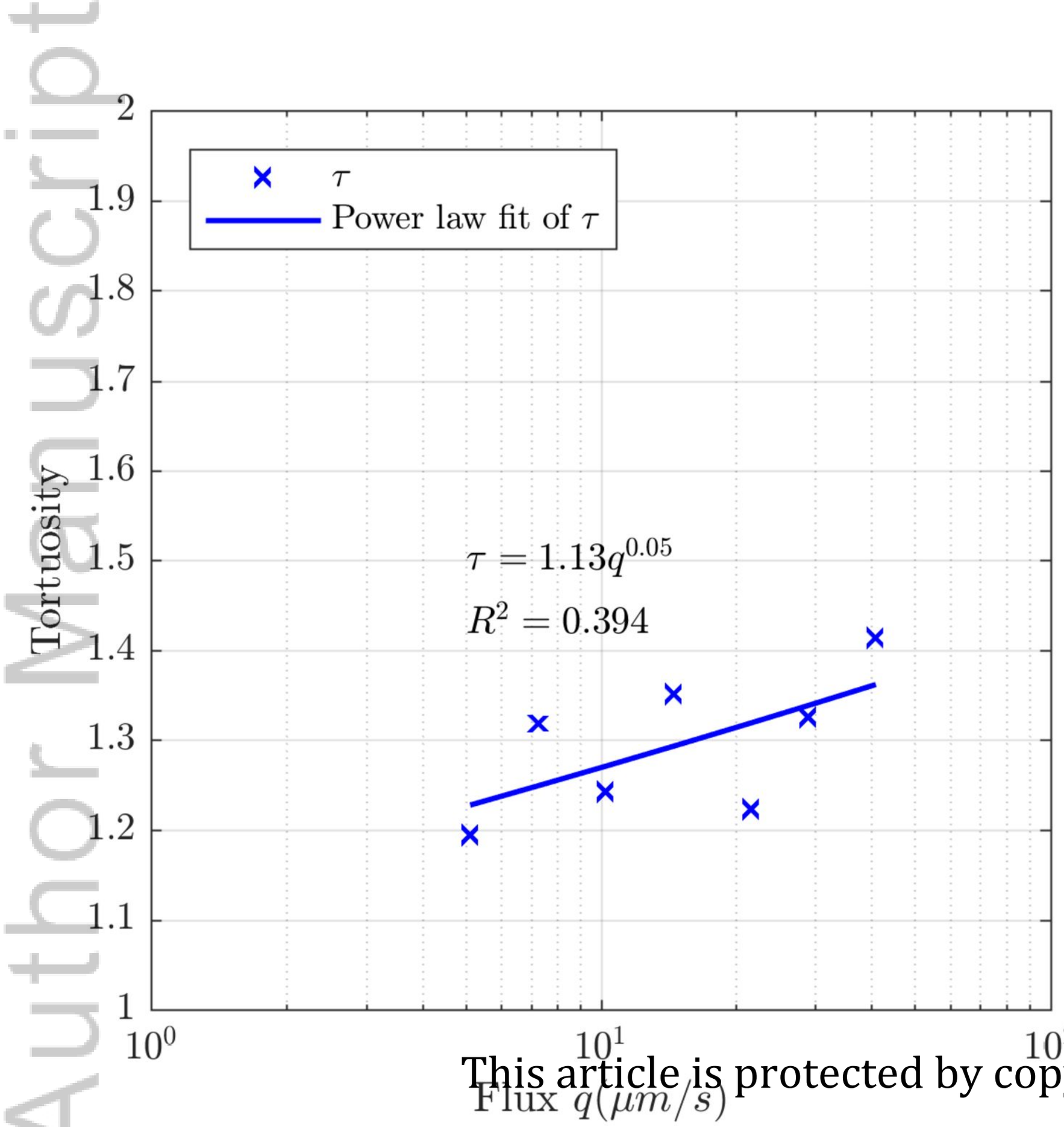

Figure 12.

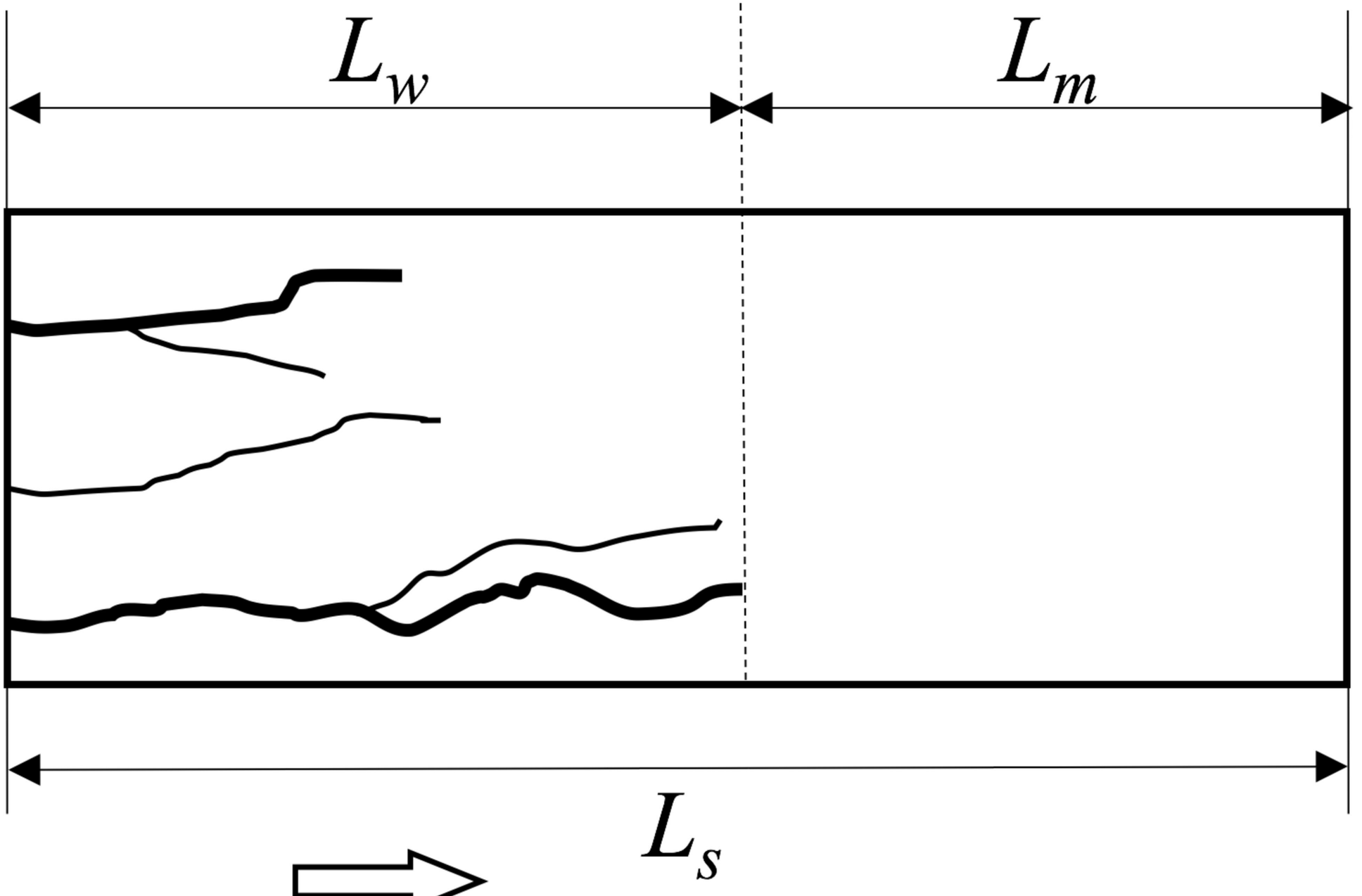

Figure 13.

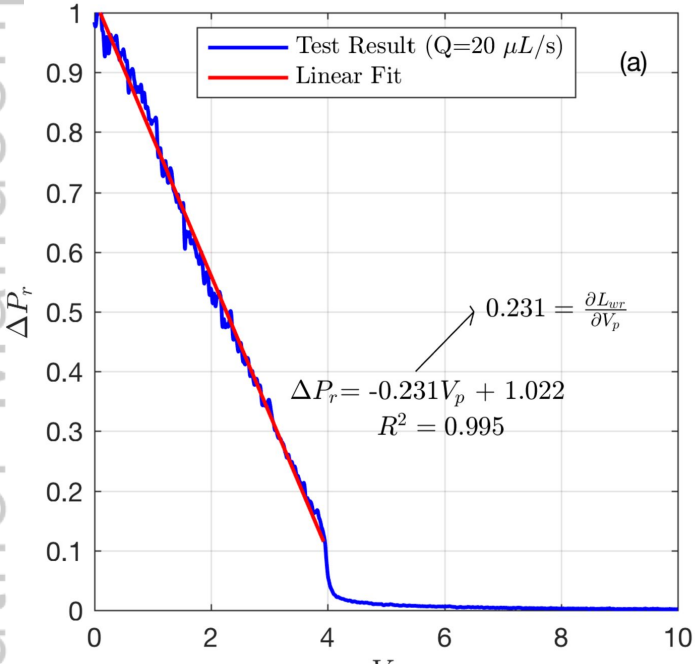

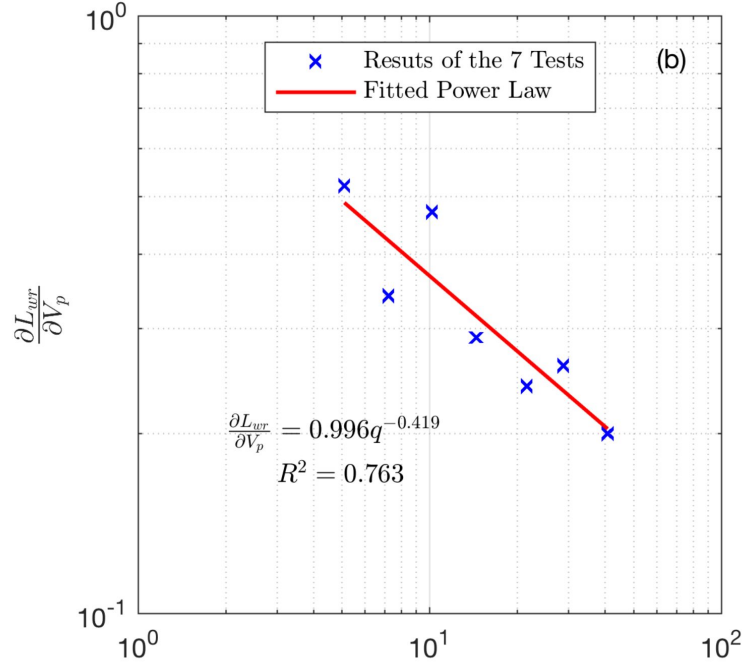

Figure 14.

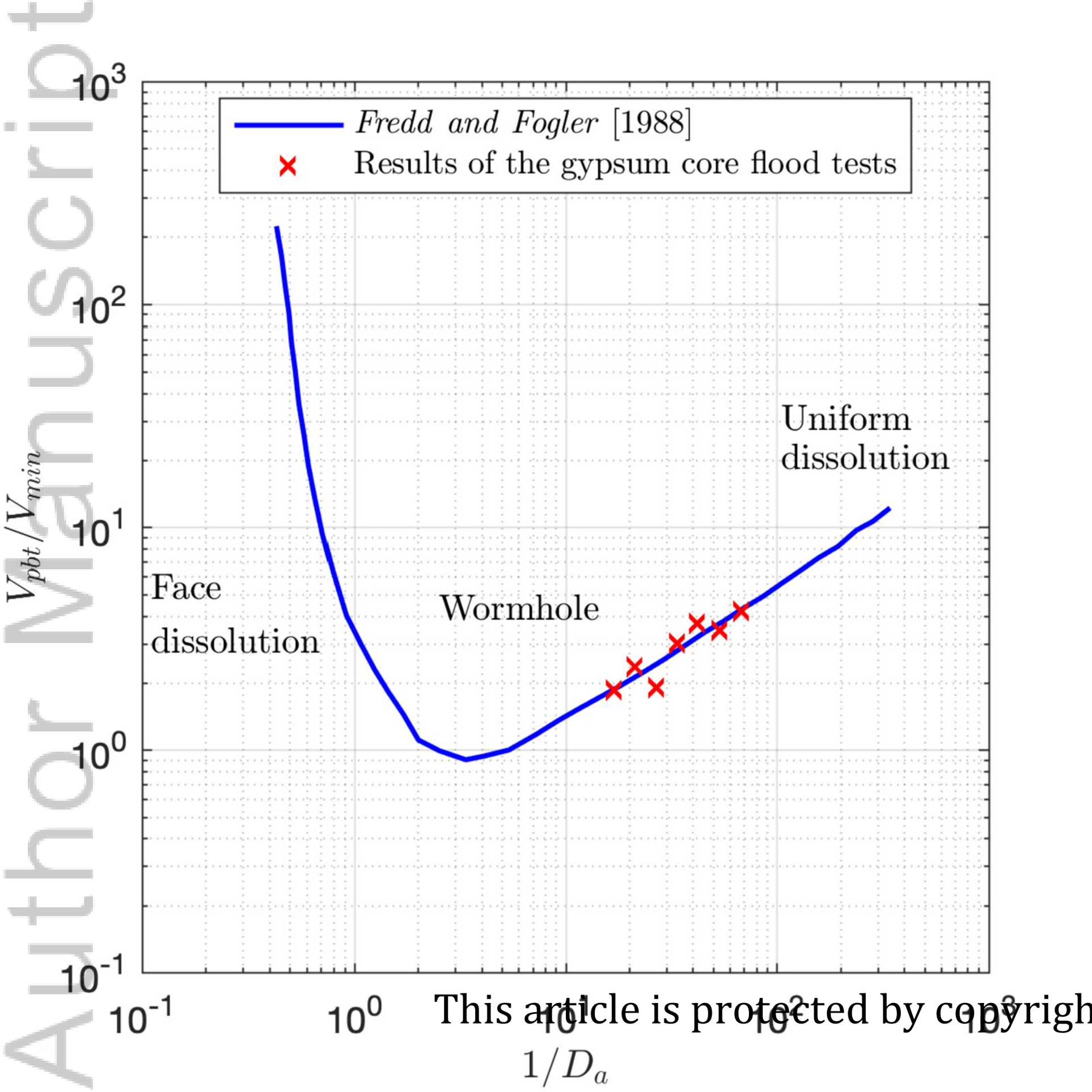

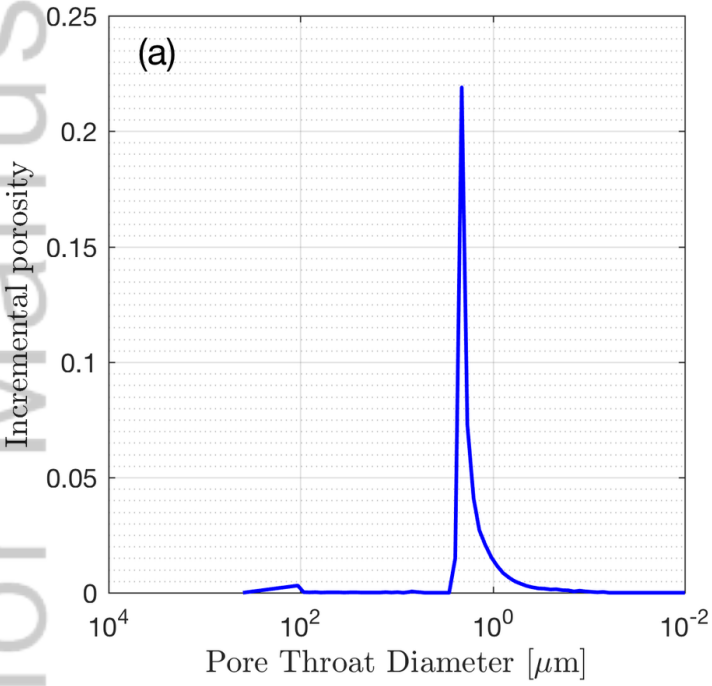

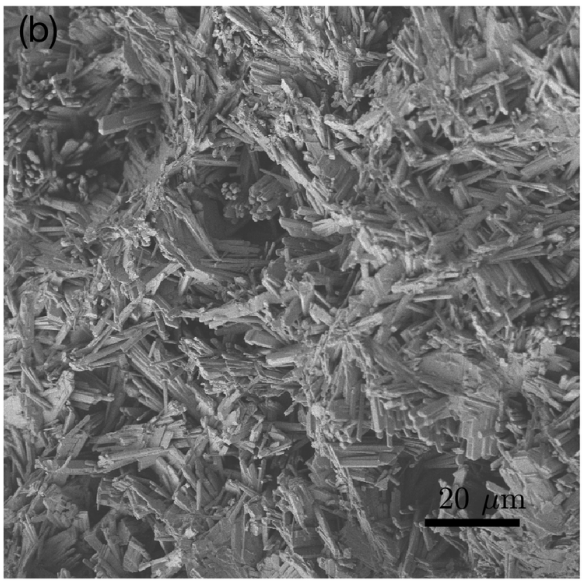

2018JB017238-f01-z-.png

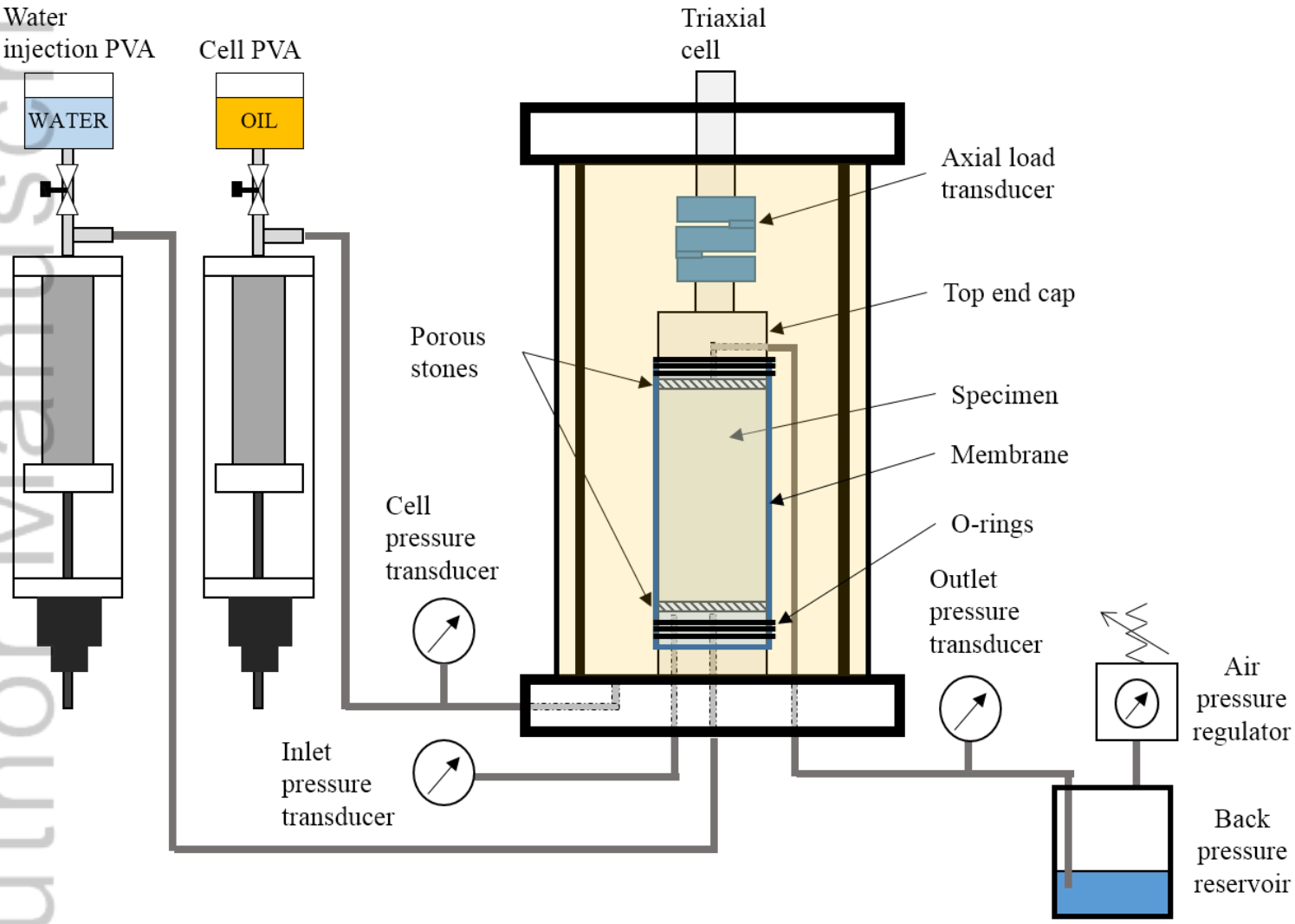

2018JB017238-f02-z-.png

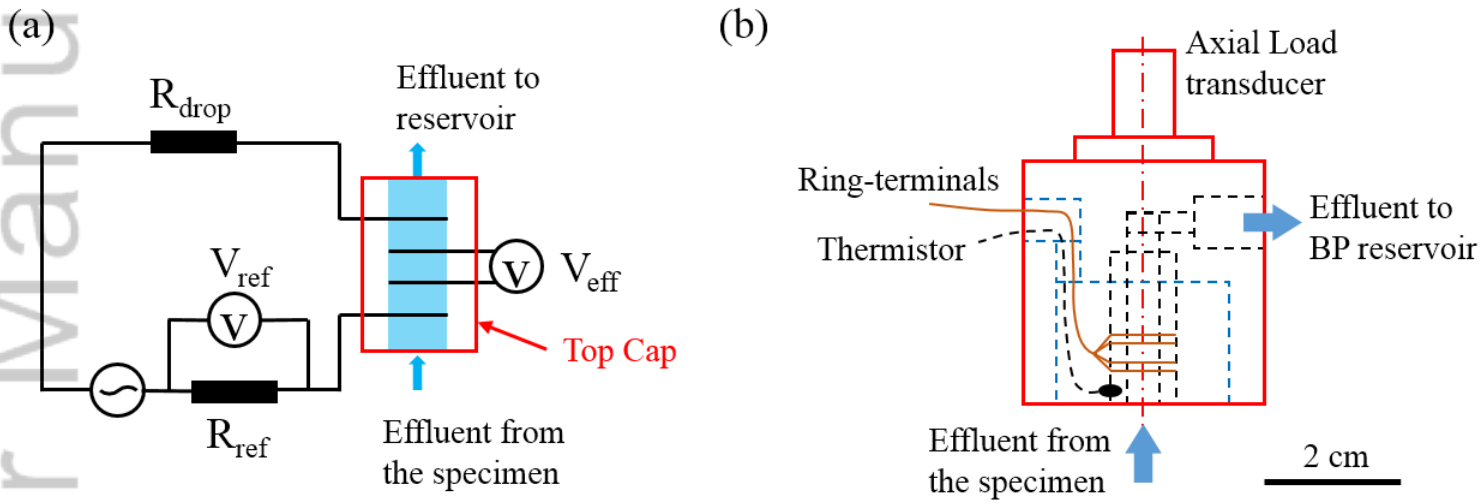

2018JB017238-f03-z-.png

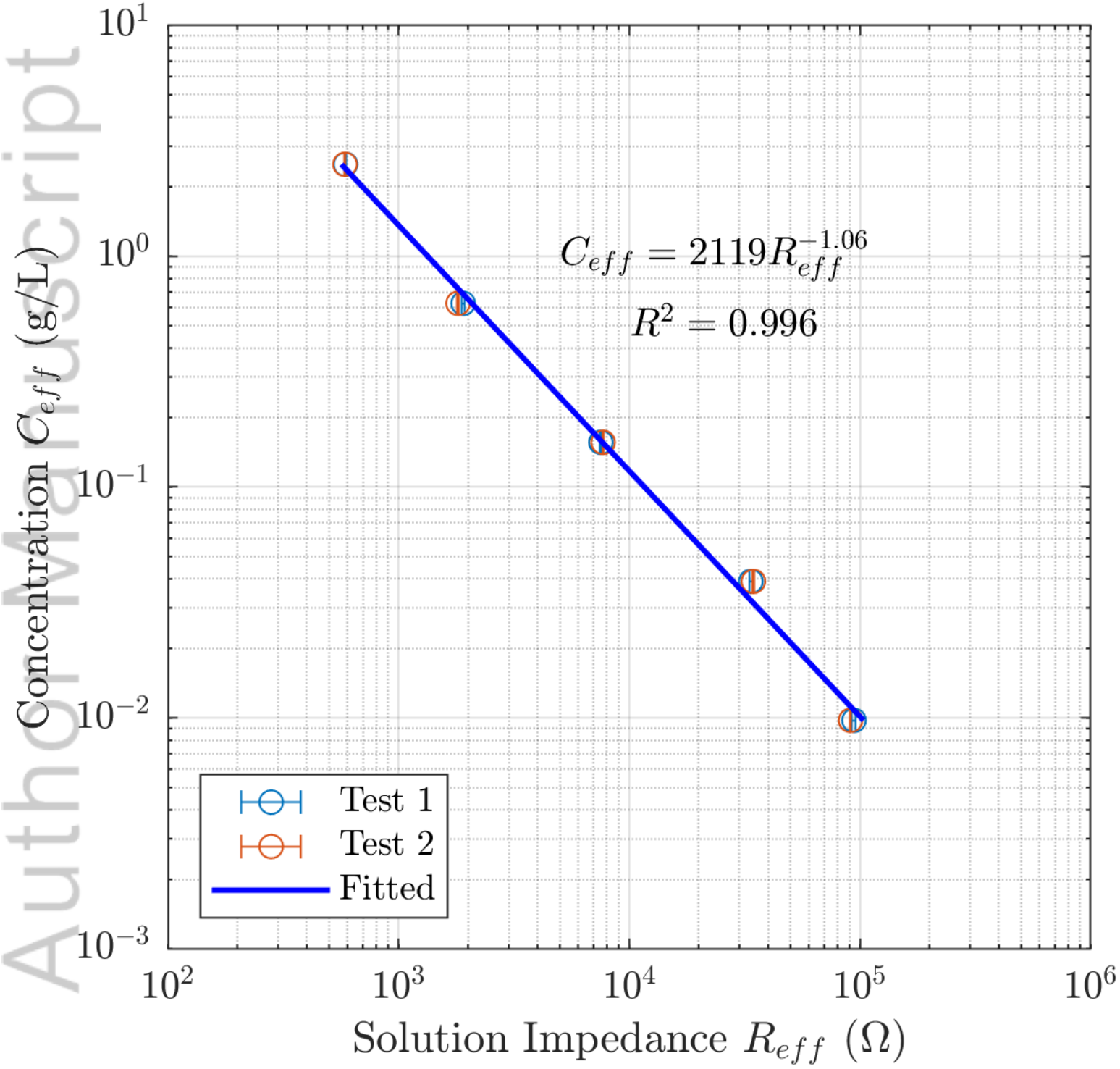

2018JB017238-f04-z-.png

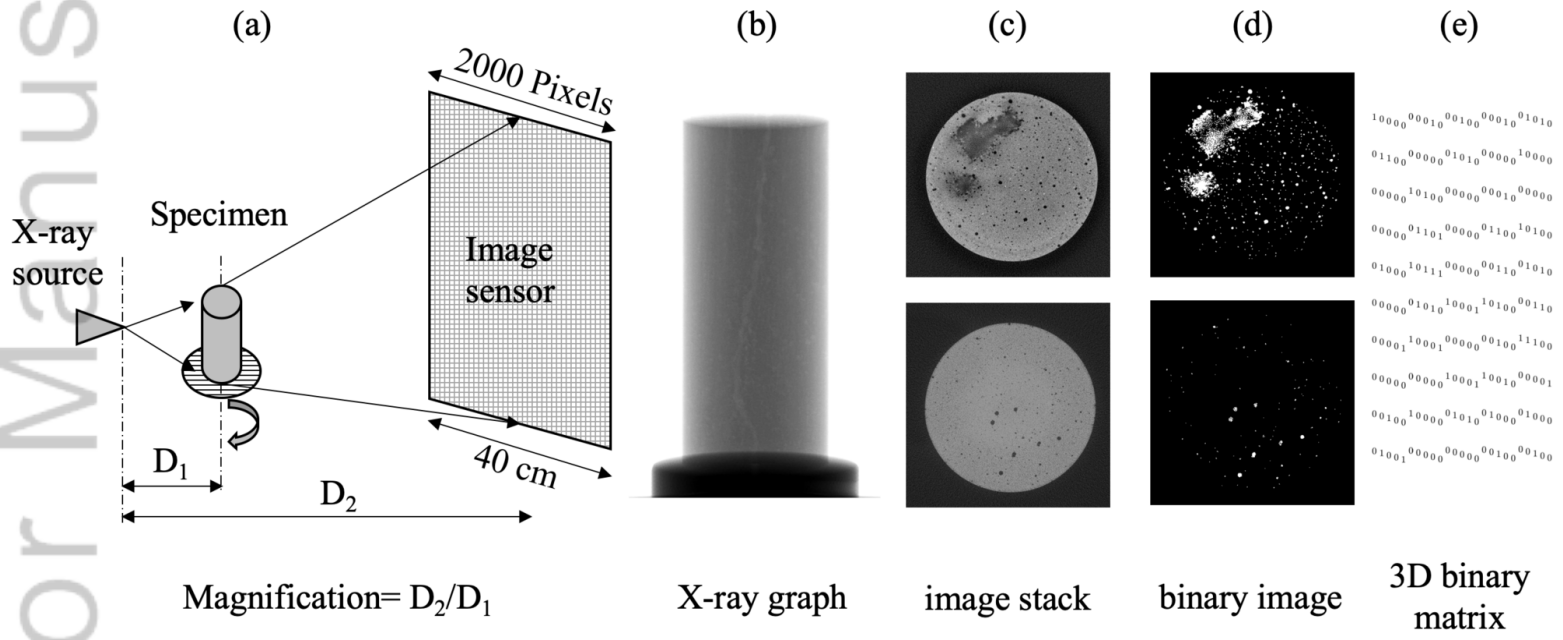

2018JB017238-f05-z-.png

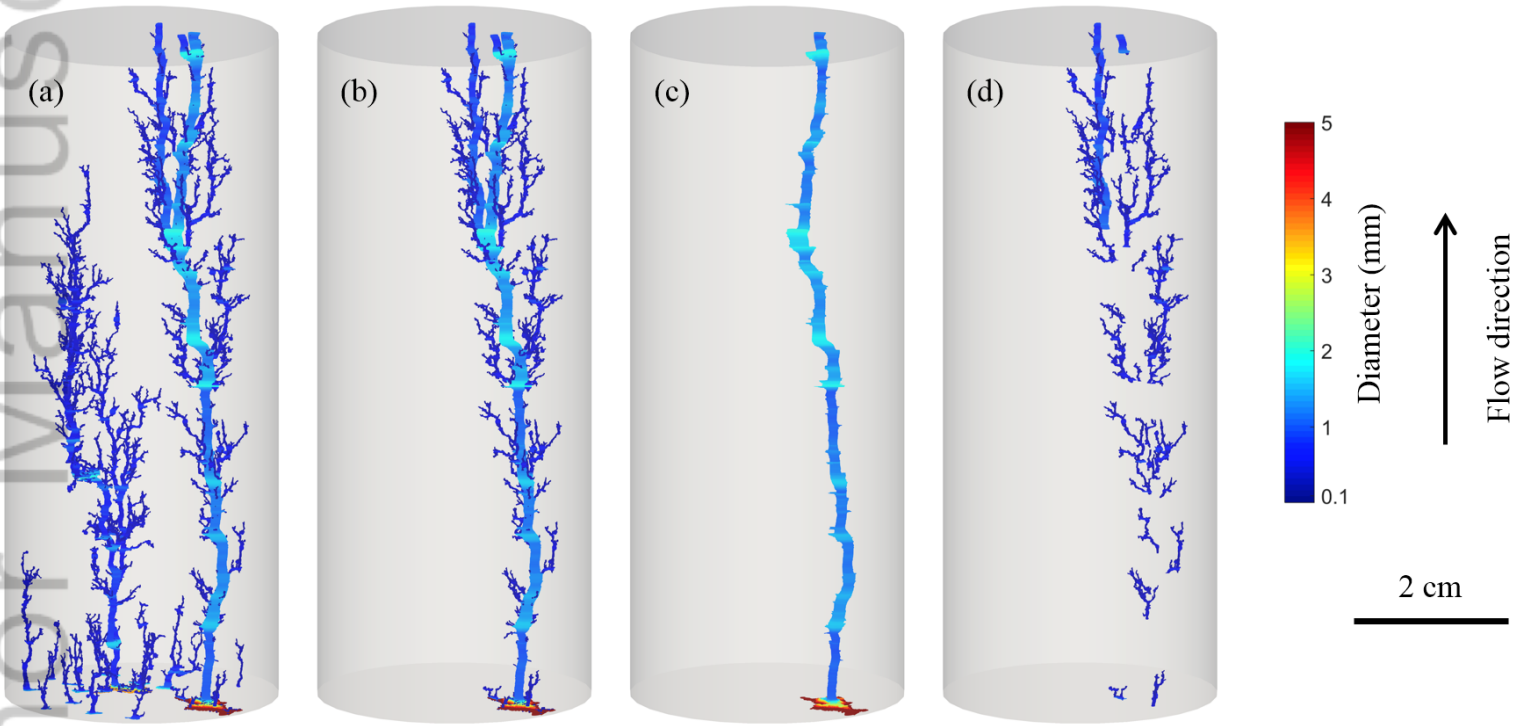

2018JB017238-f06-z-.png

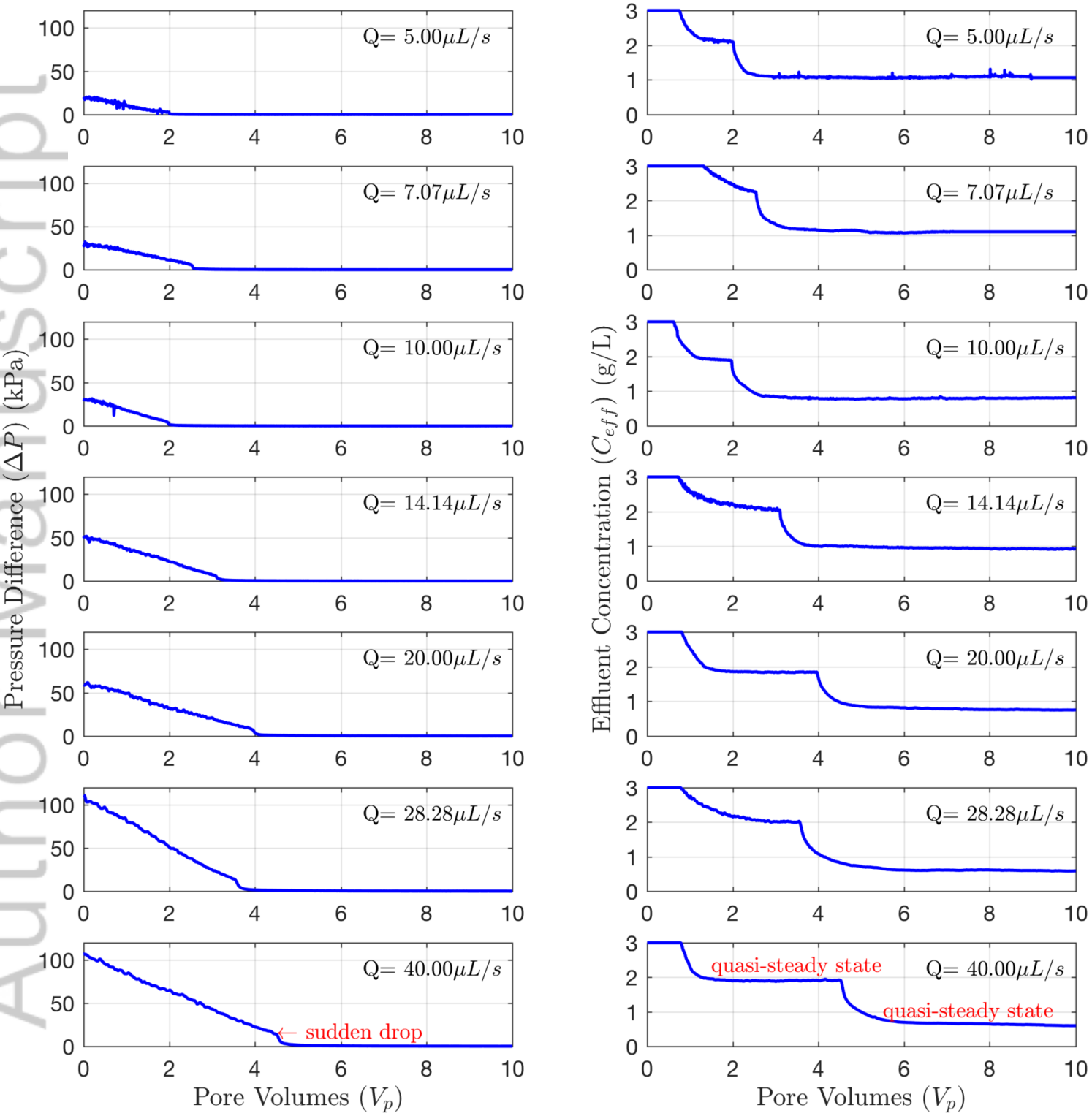

2018JB017238-f07-z-.png

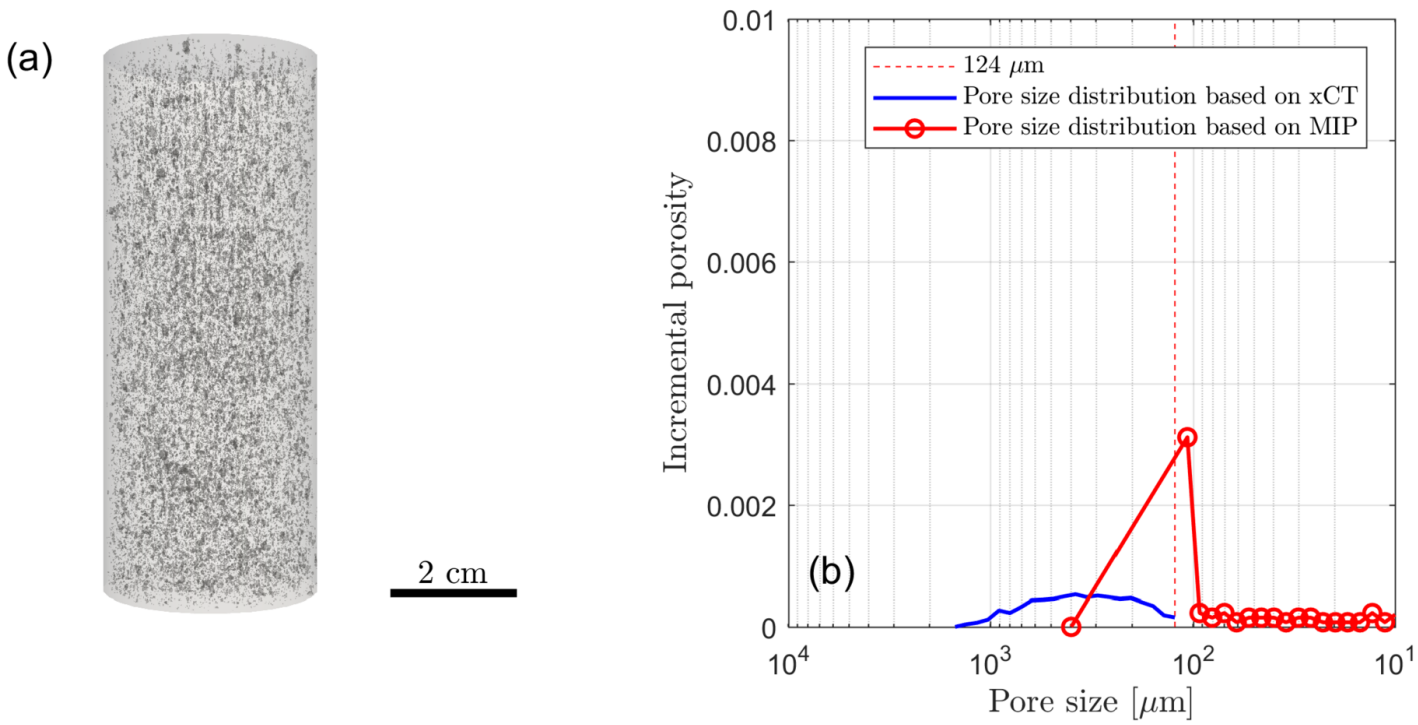

2018JB017238-f08-z-.png

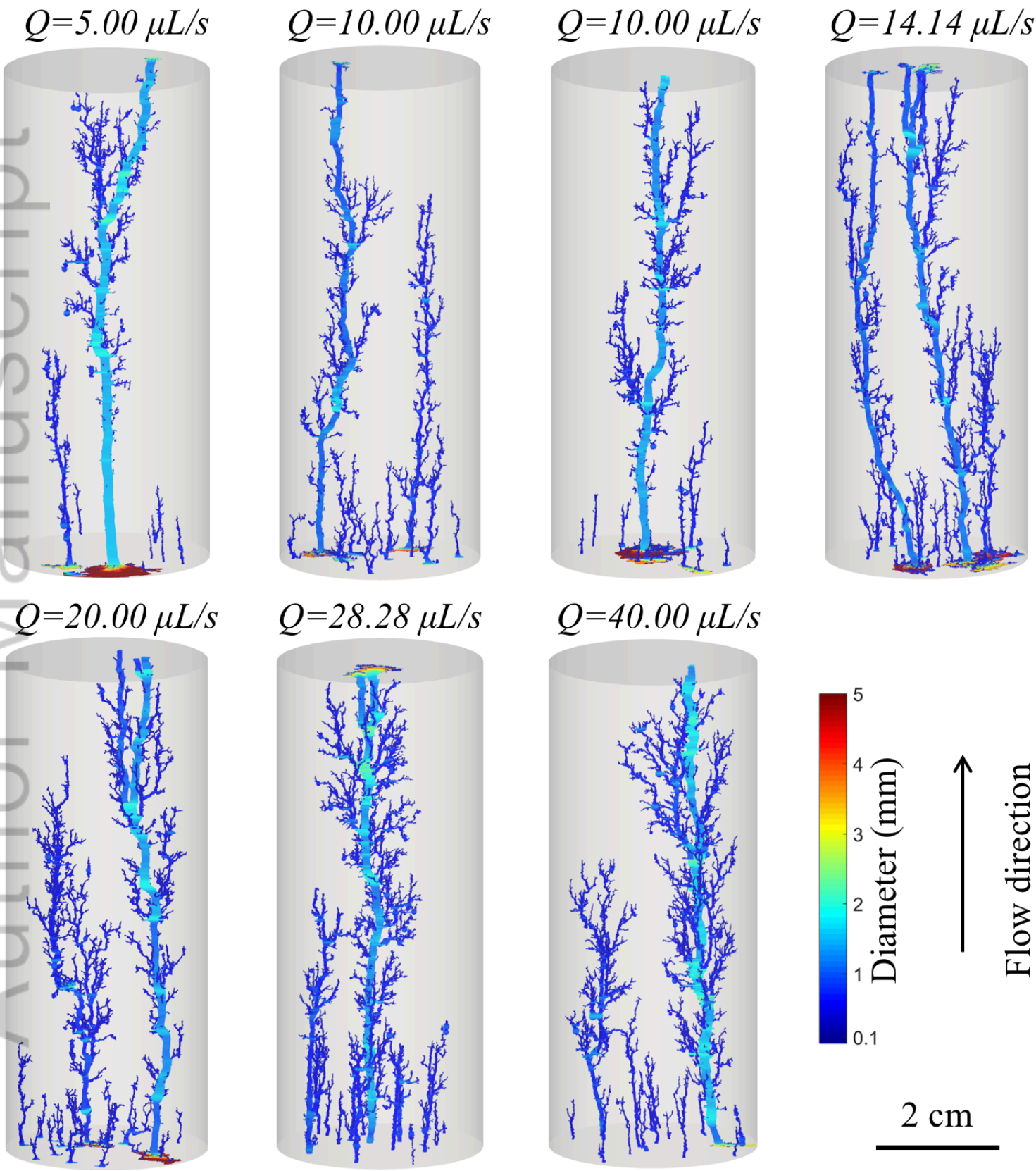

2018JB017238-f09-z-.png

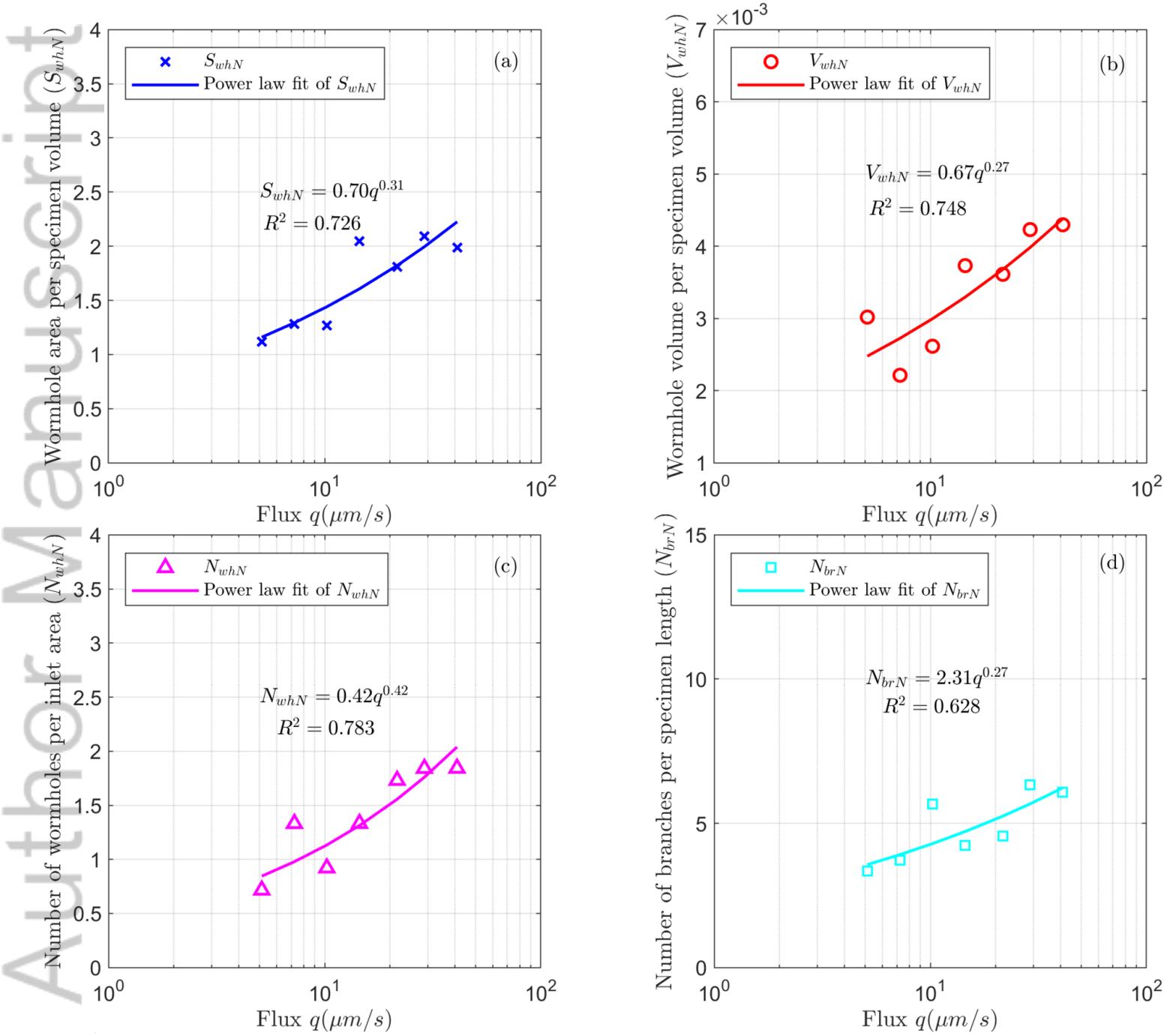

2018JB017238-f10-z-.png

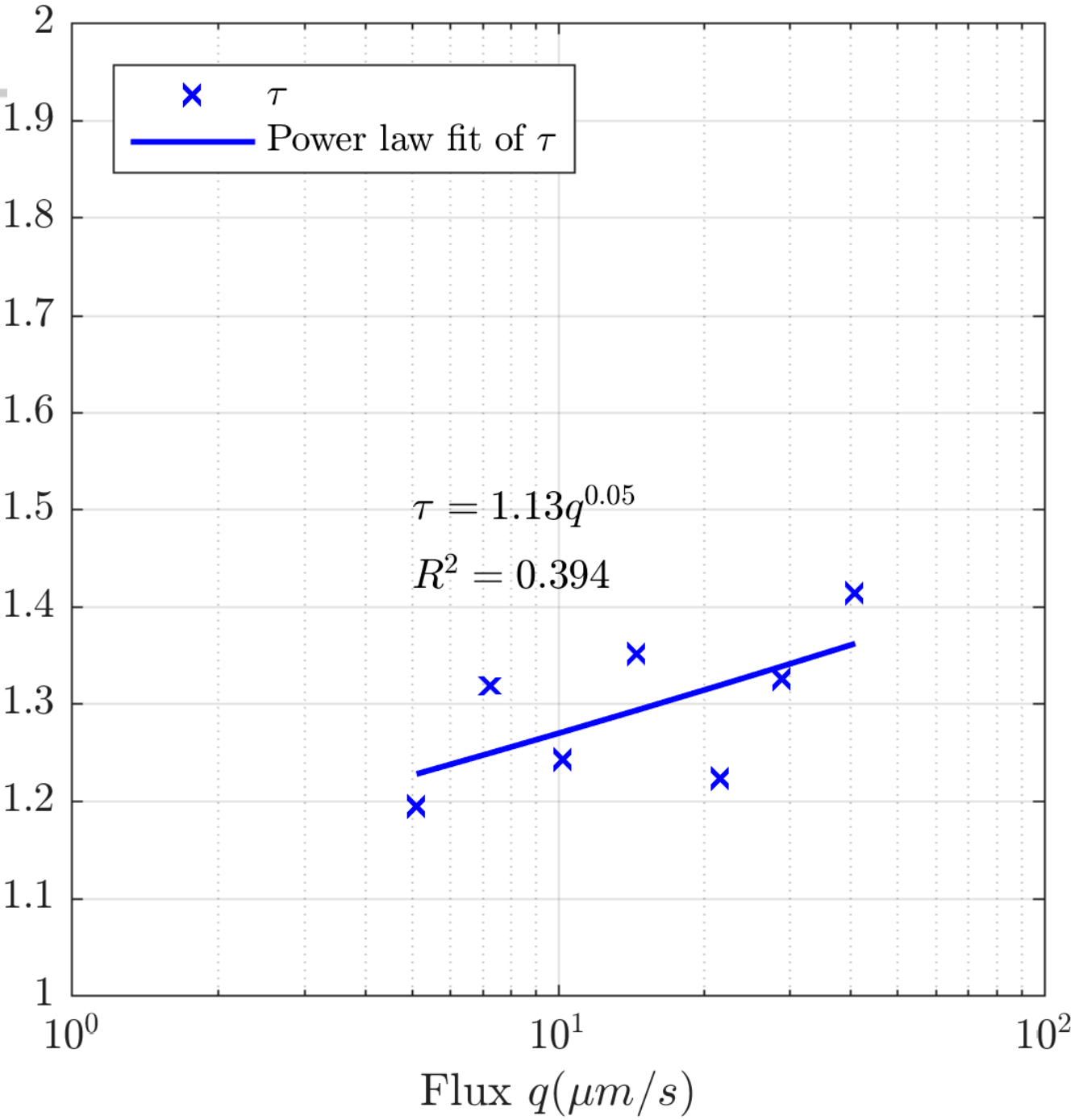

2018JB017238-f11-z-.png

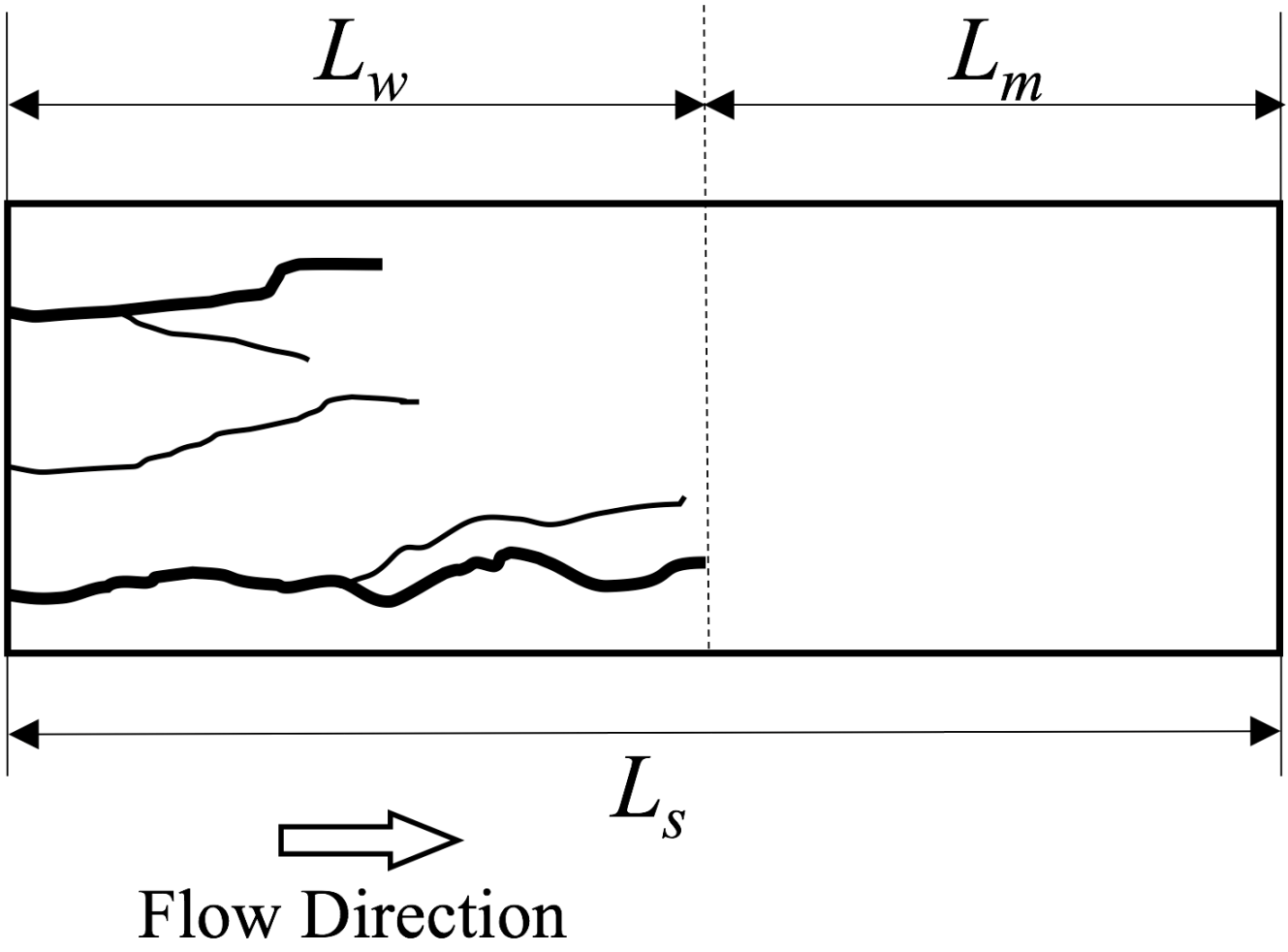

2018JB017238-f12-z-.png

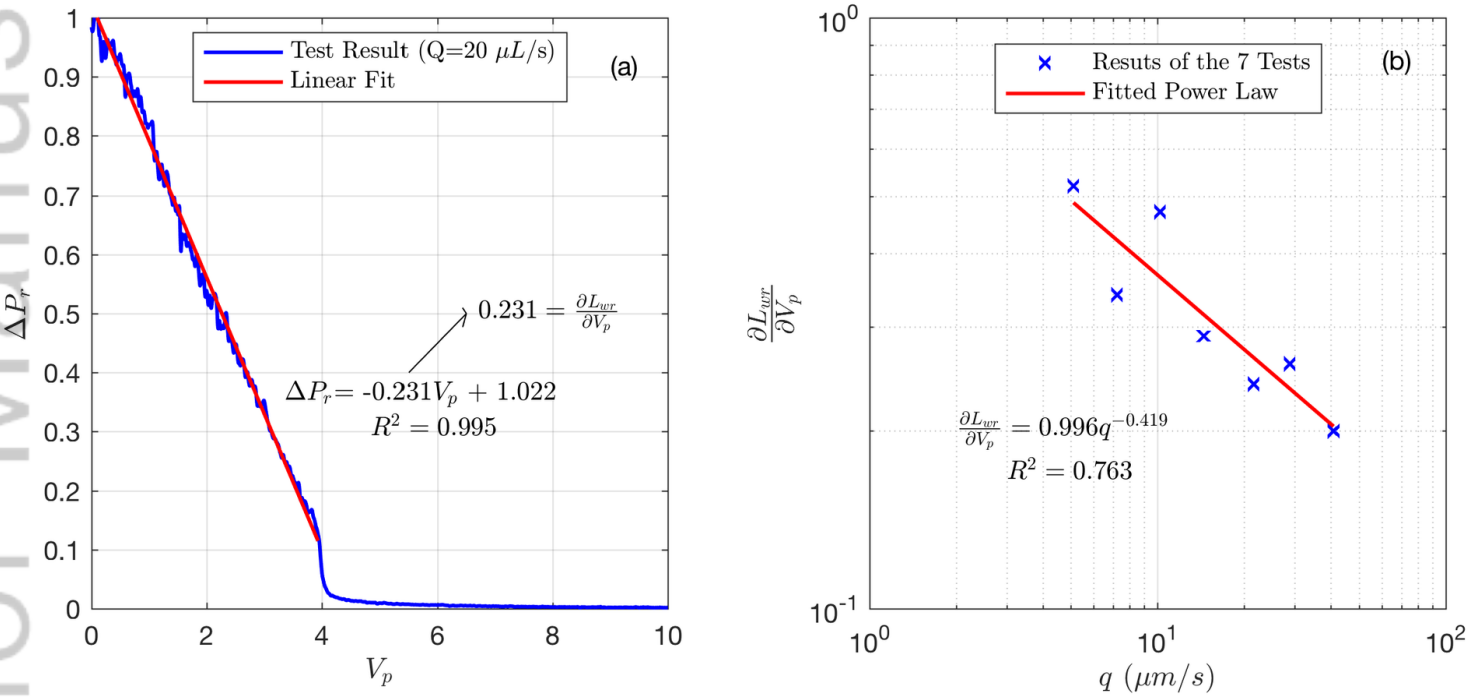

2018JB017238-f13-z-.png

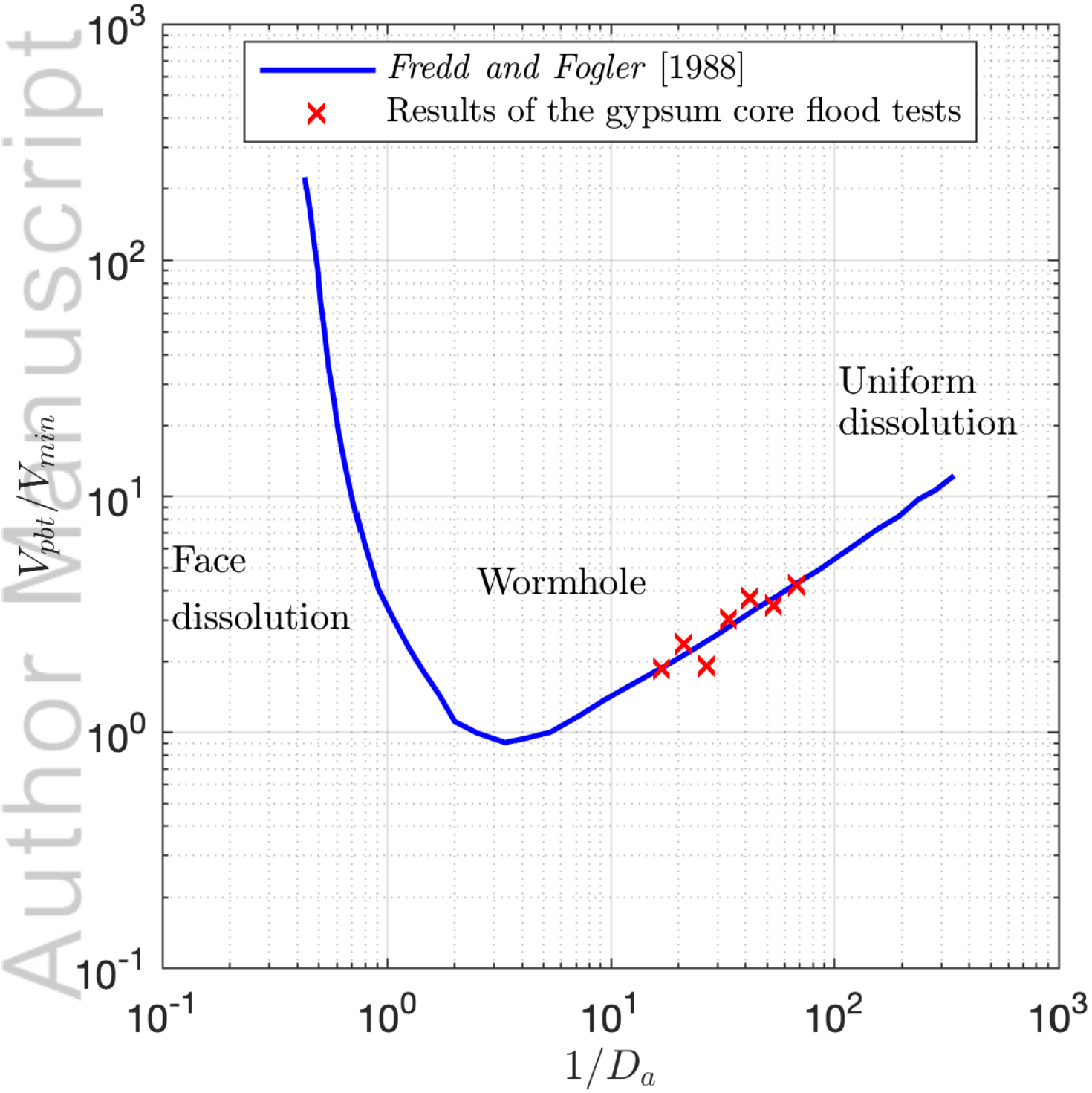

2018JB017238-f14-z-.png